Applied Thermal Engineering 233 (2023) 121122

Contents lists available at ScienceDirect

Applied Thermal Engineering

journal homepage: www.elsevier.com/locate/apthermeng

Research Paper

Enhanced heat transfer in a microchannel with pseudo-roughness induced by Onsager-Wien effect

R. Deepak Selvakumar [a,b], Daeyoung Kong [b], Hyeon Kyun Lee [b], Chirag R. Kharangate [c], Jaiyoung Ryu [d,1,*], Hyoungsoon Lee [b,e,2,*]

[a] Department of Nuclear Engineering, Khalifa University, Abu Dhabi, United Arab Emirates
[b] School of Mechanical Engineering, Chung-Ang University, Seoul, South Korea
[c] Mechanical and Aerospace Engineering Department, Case Western Reserve University, Cleveland, OH, USA
[d] School of Mechanical Engineering, Korea University, Seoul, South Korea
[e] Department of Intelligent Energy and Industry, Chung-Ang University, Seoul, South Korea

ARTICLE INFO

Keywords:
Electrohydrodynamics
Microchannel
Heat transfer
Onsager-Wien effect
Electronic cooling

ABSTRACT

A three-dimensional numerical analysis of flow and conjugate heat transfer in a microchannel in the presence of the electric-field-induced Onsager–Wien effect is performed. A novel design is proposed to induce a pseudo-roughness effect in the microchannel and thereby increasing the heat transfer. A series of thin plate electrode pairs are flushed along the bottom wall of the microchannel. The electric-field-enhanced dissociation of ions induces the Onsager–Wien effect, and generates small flow vortices near the bottom wall of the channel. These flow vortices with sharp local velocity gradients effectively disrupt the viscous and thermal boundary layers, and thus, introduce a pseudo-roughness effect. This disruption of the boundary layers improves the heat transfer between the channel wall and the working fluid. The thermal and hydraulic performances in the microchannel are quantified as a function of the flow Reynolds number (Re) and electric Reynolds number (Re_{EL}). In general, the performance factor PF is higher when the flow and electric Reynolds numbers are higher. However, the associated pressure drop penalty reduces the PF ($PF < 1$) in viscous-effect-dominated flows at $Re = 250$. By contrast, the Onsager–Wien effect increases the PF to a maximum value of 1.26 in inertia-dominated flows at $Re = 1000$ and $Re_{EL} = 15$. A significant heat transfer enhancement is realized, even at a low applied voltage of $\sim$1 kV. The results of this study indicate that the pseudo-roughness produced by the electric-field-induced Onsager–Wien effect can substantially enhance the heat transfer in a microchannel with a trivial amount of additional power consumption. Results presented in this study will serve as a benchmark to design microchannels with enhanced heat transfer by using active vortex generation based on Onsager-Wien effect.

1. Introduction

The recent trend of miniaturization, thinness, and lightness in electronic devices result in high-density heat fluxes. High heat flux generation over a small surface area leads to overheating, poor performance, and malfunctioning of electronic devices. For these reasons, it is important to develop a compact, effective and efficient thermal management technique for ensuring sustainable cooling of mini/micro-scale electronic devices [1]. Commonly used heat transfer technologies such as conventional heat sinks, pin fin arrays, fan-assisted heat sinks cooled by air have limited heat transfer capability and are unsuitable for incorporation into mini/micro-scale electronic devices [2]. Microchannels are an attractive option for the thermal management of small-sized power electronic devices. The large surface-area-to-volume ratio of microchannels helps to effectively dissipate heat from localized hotspots, and their small size makes them easier to incorporate into compact electronic devices [3]. However, owing to small dimensions and low Reynolds number flows in microchannels, the flows in them are

* Corresponding authors at: School of Mechanical Engineering, Korean University, Seoul, South Korea (J.R.). School of Mechanical Engineering, Chung-Ang University, Seoul, South Korea (H.L.).
E-mail addresses: jryu@korea.ac.kr (J. Ryu), leeh@cau.ac.kr (H. Lee).
[1] URL: https://cfdlab.korea.ac.kr/.
[2] URL: https://atsla.cau.ac.kr/.

https://doi.org/10.1016/j.applthermaleng.2023.121122
Received 1 October 2022; Received in revised form 20 May 2023; Accepted 4 July 2023
Available online 8 July 2023

generally laminar. Thus, the resultant mixing and heat transfer in a straight microchannel is limited by the viscous and thermal boundary layers [4,5].

Heat transfer enhancement in microchannels has been studied extensively in the last two decades [6–9]. Researchers have proposed several passive and active techniques to enhance heat transfer in microchannels. Among them, passive techniques include surface roughness [10], pin-fins [11], flow disruption [12], channel curvature [13], re-entrant cavities [14], and fluid additives [13]. Active methods include the introduction of a secondary flow [15], vibration [16], flow pulsation [17], and application of magnetic [18] and electrostatic fields [19]. A comprehensive review of various heat transfer enhancement techniques used in microchannels are reported in literature [20–22]. In general, works on utilization of passive heat transfer enhancement techniques are popular in literature. Active methods with low energy consumption represent attractive choices for enhancing heat transfer in conventional channels, mini channels, and microchannels.

In this context, electrohydrodynamic (EHD) flow-based techniques have been used by several researchers to enhance heat transfer in channel flows [23–30]. EHD-based techniques offer several advantages such as simple design, low power consumption, quick response, lack of moving parts, lack of noise and vibration, durability, and easy incorporation into electronic devices. All of the above studies [23–30] that use electric field for heat transfer enhancement are based on charge injection induced EHD flows (ion-drag pumping). However, ion-drag pumping requires an extremely high electric potential to induce charge injection, which is potentially unsafe. Furthermore, continuous charge injection from the electrode, degrades the electrodes and the dielectric medium. Thus, ion-drag pumping-based EHD flow techniques are less reliable, inconsistent, and unsuitable for continuous operation over a long period of time.

In contrast, EHD conduction pumping is based on Onsager-Wien effect, that occurs at weak/medium electric fields which makes it safe for operation and less power consuming. In addition, the problem of electrode and dielectric fluid deterioration is avoided in EHD conduction pumping. EHD flow due to the Onsager–Wien effect is very less explored as compared to ion-drag pumping. Atten and Seyed-Yagoobi [31] proposed the theoretical model for the Onsager–Wien-effect based EHD conduction pumping flow. Extending their pioneering work, several works on analytical and numerical modelling of EHD conduction pumping were carried out by other researchers [32–35]. Lin and Jang [36] numerically studied flow and heat transfer by means of EHD conduction pumping in a microchannel. EHD conduction pumping generated a flow that was adequate to dissipate heat fluxes of up to 2.5 W/cm^2. An experimental study by Pearson and Yagoobi [37,38] showed that EHD conduction pumping can increase heat transfer in single and two-phase microchannel flows. However, their results showed that stand-alone EHD conduction pump was not sufficient to achieve significant heat dissipation. Patel and Seyed-Yagoobi [39] developed an EHD conduction micropump to assist two-phase flow in a microchannel. The additional flow produced by the EHD pump effectively prevented evaporator dry out. Pearson [40] experimentally studied the capability of EHD conduction pumping to introduce a secondary flow in a microcapillary device. The secondary flow induced by EHD conduction pumping enhanced single and two-phase heat transfer in the microcapillary tube. A numerical study by Selvakumar et al. [41] employed EHD conduction pumping for heat transfer intensification in electronic cooling applications. Thermal boundary layer and enhanced heat transfer up to 31.2 % were achieved by EHD vortices generated by Onsager-Wien effect. Nourdanesh et al. [42] performed an experimental study on heat transfer enhancement in an open-channel flow with a EHD conduction pump. EHD conduction pumping resulted in heat transfer enhancement at lower applied voltages. Higher applied voltages had a negative impact on the heat transfer. Jafari et al. [43] experimentally investigated the effect of temperature on performance of EHD conduction pumping. The difference in ion mobility caused by the temperature difference resulted in increased flow rate. A numerical study on heat transfer enhancement by EHD conduction pumping in an inclined macro-channel showed that electrode width and applied voltage are important parameters that determine the efficiency of heat transfer enhancement by EHD conduction pumping [44]. Very recently, Du et al. [45] reported an experimental study of EHD conduction pumping used for heat transfer enhancement in a channel. A maximum of 21.9 % increase in heat transfer is obtained at the maximum applied voltage of 12 kV.

From the above literature review, it is evident that all the previous research works aimed to use Onsager-Wien effect in microchannels attempted to use EHD conduction pumping flow as the main driving force for fluid flow. Although several promising results were reported, it can be inferred that EHD conduction pumping alone cannot induce a flow rate that is adequate for dissipating high-density heat fluxes of $\geq 100 W/cm^2$, as encountered in power electronic devices [36–38]. In this context, we propose a new design to use the Onsager–Wien effect to induce pseudo-roughness in a microchannel. To the best of our knowledge, this is the first study to utilize Onsager-Wien effect to induce pseudo-roughness in a microchannel. A numerical investigation is performed to evaluate the influence of small vortices induced by the Onsager–Wien effect on the heat transfer in a straight rectangular microchannel. The mechanism of the boundary layer disruption due to the EHD vortices is highlighted. The flow and heat transfer characteristics are studied for different strengths of external flow and electric potentials.

2. Problem formulation

2.1. Computational domain

Fig. 1 presents the computational domain consisting of a microchannel with an overall length $L = 10mm$, width $W = 0.3mm$, and height $H = 0.35mm$. The width and height of fluid passage in the channel is $W_C = 0.1mm$ and $H_C = 0.2mm$, respectively. The thickness of the channel substrate base is $H_S = 0.15\ mm$ and the sidewall thickness is $W_W = 0.1mm$. The bottom wall of the channel's fluid passage is flushed with thin electrode plates. A total of 16 electrode pairs (EPs) are considered, where each pair consists of one high-voltage electrode and a grounded electrode. The width of all the electrodes is equal to the channel passage width $W_C = 0.1mm$. The length of the high-voltage electrode is $L_H = 0.1mm$, and the length of the grounded electrode is $L_G = 0.30\ mm$. The high-voltage electrodes are shorter than the grounded electrode so as to create a difference in surface area between the electrodes, which is essential for generating a net fluid motion. The electrodes are distributed uniformly along the bottom wall of the channel passage, and the distance between two consecutive electrodes is $D = 0.10mm$. The dimensions and positioning of the electrodes are shown in the top view of the bottom wall of the microchannel's fluid passage (see the inset of Fig. 1).

2.2. Governing equations

The numerical model [41,46] of the flow and temperature fields in the fluid region is based on the following assumptions:

1) The flow is three-dimensional, laminar, Newtonian and incompressible.
2) The viscosity of the working fluid is considered to be temperature-dependent [47].
3) Viscous dissipation, radiation and Joule heating are neglected [48].

Based on the above assumptions, the flow in the fluid region is governed by the incompressible Navier-Stokes equations, as shown in

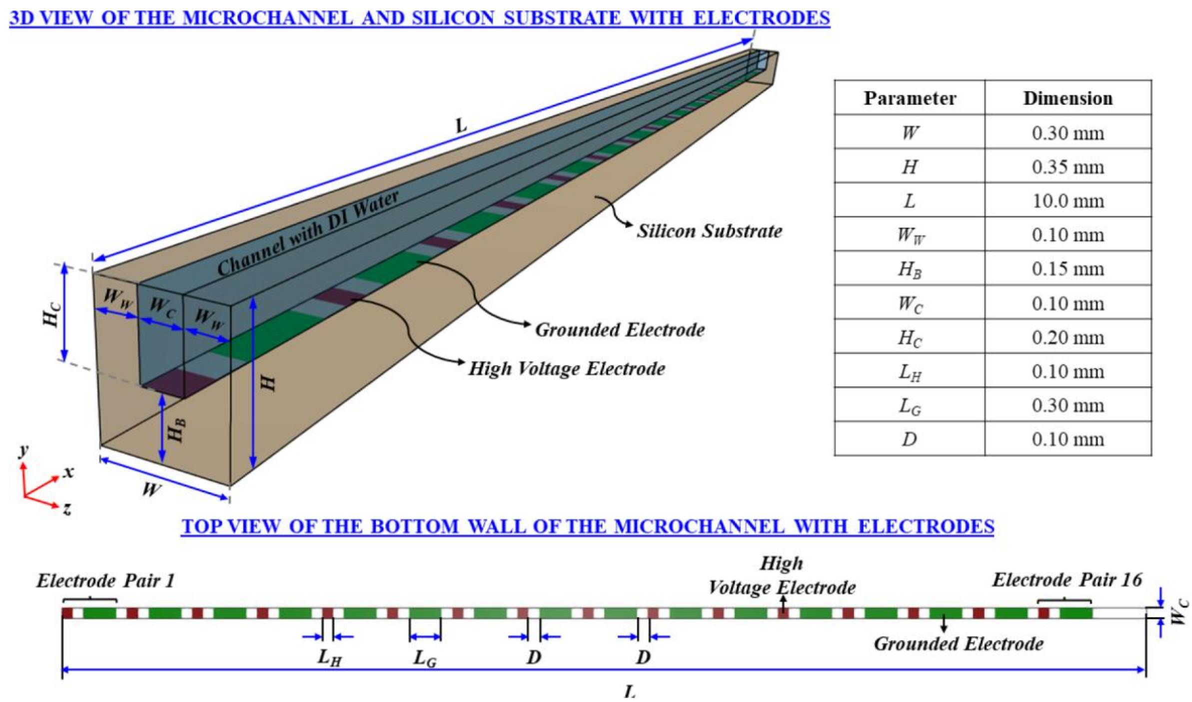

Fig. 1. Schematic representation of the computational domain.

Eqs. (1) and (2):

$$\nabla.\vec{u} = 0 \tag{1}$$

$$\frac{\partial \vec{u}}{\partial t} + \nabla.(\vec{u}\vec{u}) = -\nabla P + \upsilon_f \nabla^2 \vec{u} + \vec{F}_E \tag{2}$$

Here, $\vec{u}$ represents the velocity vector, P is the pressure, and υ_f is the kinematic viscosity of the fluid. The temperature field in the fluid region is obtained by solving the energy equation given in Eq. (3).

$$\frac{\partial T}{\partial t} + \vec{u}.\nabla T = \nabla.(\alpha_f \nabla T) \tag{3}$$

In Eq. (3), T is the temperature, and α_f is the thermal diffusivity of the working fluid. The temperature distribution in the solid region is given by Eq. (4), as follows:

$$\frac{\partial T}{\partial t} - \nabla.(\alpha_s \nabla T) = 0 \tag{4}$$

The body force term $\vec{F}_E$ due to electric field in Eq. (2) can be expressed as follows [49,50]:

$$\vec{F}_E = q_c \vec{E} - \frac{1}{2}\left(\vec{E}.\vec{E}\right)\nabla \varepsilon_f + \frac{1}{2}\nabla\left[\vec{E}^2\left(\frac{\partial \varepsilon_f}{\partial \rho}\right)\rho\right] \tag{5}$$

The right-hand side of Eq. (5) consists of three terms, namely (i) Coulomb force, (ii) dielectrophoretic force, and (iii) electrostriction force. In an incompressible, single-phase fluid with poor temperature-dependent dielectric permittivity, the dielectrophoretic force and electrostriction force terms become zero. Thus, only the Coulomb force $q_c\vec{E}$ is considered in the present study. The electric field $\vec{E}$ in the liquid region is calculated based on the divergence of electric potential as $\vec{E} = -\nabla V$. The distribution of electric potential V is given as follows:

$$\nabla.(\varepsilon_f \nabla V) = -q_c \tag{6}$$

Here, ε_f represents the dielectric permittivity of the fluid, and $q_c = p - n$ is the net space charge density. p and n are the positive and negative charge densities, respectively. The conservation of the positive and negative charge species under the influence of an external electric field is expressed using the following set of equations [34]:

$$\frac{\partial p}{\partial t} + \nabla.\left[\vec{u}p + K\vec{E}p - D\nabla p\right] = R_p \tag{7}$$

$$\frac{\partial n}{\partial t} + \nabla.\left[\vec{u}n - K\vec{E}n - D\nabla n\right] = R_n \tag{8}$$

In the above equations, K and D denote the ionic mobility and ionic diffusivity of the fluid, respectively. The source terms R_p and R_n denote the reaction terms for positive and negative charges, respectively.

The model for EHD conduction phenomenon used in this study is adopted from the theoretical model proposed by Atten and Yagoobi [31]. In the absence of electric field or in the presence of weak electric field, the neutral species (AB) in the dielectric fluid dissociate into positive (A^+) and negative charges (B^-), which is followed by complete recombination of the (A^+) and (B^-) to form the original neutral species (AB).

$$AB \underset{k_r}{\overset{k_d}{\rightleftarrows}} A^+ + B^- \tag{9}$$

Here, k_d and k_r are the dissociation and recombination rate constants, respectively. In other words, the dissociation and recombination processes are in dynamic equilibrium i.e., the rate of dissociation of neutral molecules is equal to the rate of recombination of positive and negative charges. This can be mathematically expressed as

$$k_{d(eq)}N_{eq} = k_{r(eq)}p_{eq}n_{eq} \tag{10}$$

Here, N is the concentration of neutral molecules. p and n are the charge densities of positive and negative charge species, respectively. The subscript "eq" represents the equilibrium condition. The charge densities of positive and negative ions under the equilibrium conditions are expressed as follows [34]:

$$p_{eq} = n_{eq} = N_{eq} = \frac{\sigma}{2K} \tag{11}$$

Here, σ is the electrical conductivity of the fluid. From Eqs. (10) and (11),

$$k_{d(eq)} = k_{r(eq)} N_{eq} \quad (12)$$

The rate of recombination is given by the Langevin's formula [51] as

$$k_{r(eq)} = \frac{2K}{\varepsilon_f} \quad (13)$$

According to Onsager's model [49,52], electric-field enhanced dissociation takes place by increasing the external electric strength beyond a critical value. Thus, in the presence of Onsager-Wien effect (electric-field enhanced dissociation) k_d exceeds $k_{d(eq)}$. According to the Onsager model [53],

$$k_d = k_{d(eq)} F(b) \quad (14)$$

Here, $F(b)$ is the Onsager function for field-enhanced dissociation. Moreover, $b^2 = (l_B/l_0)^2 = 4\gamma \overrightarrow{E}, \gamma = e^3/16\pi\varepsilon_f k_B^2 T^2$, and $F(b) = I_1(2b)/b$. The Onsager distance $\left(l_0 = \sqrt{e/4\pi\varepsilon \overrightarrow{E}}\right)$ is the distance in which the force due to the external field is countered by the Coulomb force of the ion pair [53]. $l_B = e^2/4\pi\varepsilon_f k_B T$ is the Bjerrum distance [52], k_B is Boltzmann's constant, and e is the elementary electric charge. The function I_1 is a modified Bessel function of first kind and order one [49,52,53]. In an ascending series, the function I_1 can be expanded as $I_1(x) = \sum_{k=0}^{\infty} \frac{(x/2)^{1+2k}}{k!(k+1)!}$.

The reaction terms R_p and R_n in Eqs. (7) and (8) account for the dissociation and recombination reactions and can be mathematically expressed as [52]

$$R_p = R_n = k_d N_{eq} - k_r pn \quad (15)$$

It is to be noted that k_r is not affected by Onsager-Wien effect. Hence, $k_r = k_{r(eq)}$ and $N = N_{eq}$. Finally, we get the expressions for the reaction terms (including the Onsager-Wien effect) in Eqs. (7) and (8) by substituting Eqs. (11)–(14) in Eq. (15)

$$R_p = R_n = \frac{2K}{\varepsilon_f}\left[F(b)\frac{\sigma^2}{4K^2} - pn\right] \quad (16)$$

Generally, in EHD applications, electrically insulating materials are selected as substrates. In the present study, we consider an electrical insulator as the substrate of the microchannel, and therefore, the solid region is devoid of free charges. For this reason, charge transport in the solid region is neglected. However, the distribution of electric potential in the solid region does influence charge transport in the fluid region. Hence, only Gauss's law $(\nabla.(\varepsilon_s \nabla V) = 0)$ for electric potential distribution is solved in the solid region. In this expression, ε_s is the dielectric permittivity of the solid material.

2.3. Boundary conditions

At the interface of the fluid and solid regions, the no slip and no penetration boundary conditions are applied. At the microchannel inlet, a uniform inlet velocity in the positive x-direction U_{in} is considered. The pressure outlet boundary condition is applied at the channel outlet. The bottom wall of the microchannel base is exposed to a constant, uniform heat flux of $q_w = 1 \times 10^6 W/m^2$. The outer surfaces of the sidewalls and the entire top surface are thermally insulated. The inlet temperature of the working fluid is $T_{in} = 293.15K$. The short electrodes in the bottom wall of the fluid passage are connected to a high electric potential V. The longer electrodes are grounded $(V = 0)$. All other outer surfaces are electrically insulated. The Dirichlet boundary condition for positive ions $(p = 0)$ and the Neumann boundary condition $(\partial n/\partial y) = 0$ for negative ions are applied to the high-voltage electrodes. Likewise, the Dirichlet boundary condition for negative ions $(n = 0)$ and the Neumann boundary condition for positive ions $(\partial p/\partial y) = 0$ are applied to the grounded electrodes. The fluid-side heat transfer in the cells adjacent to the solid region (including the electrodes) is computed using Fourier's law as $-k_f(\partial T_f/\partial \widehat{n}) = -k_s(\partial T_s/\partial \widehat{n})$. Here, the subscripts "$f$" and "$s$" denote the fluid and solid regions, respectively. k is the thermal conductivity, and $\widehat{n}$ is the local coordinate normal to the surface. The boundary conditions are summarized in Table 1.

2.4. Material properties

In the present study, we consider deionized (DI) water as the working fluid and silicon as the material of the microchannel substrate. The properties of DI water and silicon are summarized in Tables 2 and 3. All properties except for fluid viscosity are constant with respect to temperature. The ionic mobility of DI water is calculated using Walden's rule [54] as $K = 1.5 \times 10^{-11}/\mu_f$. Likewise, the ionic diffusivity of DI water is calculated using Einstein's relation [55] as $D = Kk_B T_{ref}/e$. Here, μ_f is the dynamic viscosity of DI water at $T_{ref} = 293.15K$.

2.5. Governing and evaluation parameters

The governing and evaluation parameters of interest used in this study are presented in this section. In the problem considered herein, fluid motion is driven by two factors, namely (i) the base flow set by the inlet velocity and (ii) the flow vortices induced by the Onsager–Wien effect. The base flow in the microchannel is characterized by the flow Reynolds number Re, which is defined as [56,57]

$$Re = \frac{\rho_f U_{in} D_H}{\mu_f} \quad (17)$$

Here, ρ_f is the fluid density, U_{in} is the uniform inlet velocity in the positive x–direction, and $D_H = 2W_C H_C/(W_C + W_H)$ is the hydraulic diameter. The fluid motion induced by the Onsager–Wien effect is characterized by the electric Reynolds number Re_{EL}, which is defined as follows [32]:

$$Re_{EL} = \frac{\rho_f K \Delta V}{\mu_f} \quad (18)$$

The flow Reynolds number of $250 \leq Re \leq 1000$ considered herein is in the laminar regime, and the corresponding inlet velocity is $1.8803 \leq U_{in} \leq 7.5212 m/s$. Likewise, $Re_{EL} = 5$, 10 and 15 are considered herein, which correspond to applied potential differences $\Delta V = 334.6030\ V$, $669.2059\ V$ and $1003.8089\ V$, respectively. Another important parameter that determines the onset of the Onsager–Wien effect is the conduction number C_0, which is defined as follows [34]:

$$C_0 = \frac{ND^2}{\varepsilon_f \Delta V} \quad (19)$$

where N is the neutral charge distribution determined using Eq. (11).

Table 1
Boundary conditions.

Location	Condition
Fluid–solid interface	$u_x = u_y = u_z = 0; \frac{\partial V}{\partial \widehat{n}} = 0; \frac{\partial p}{\partial \widehat{n}} = 0; \frac{\partial n}{\partial \widehat{n}} = 0$
High-voltage electrodes	$u_x = u_y = u_z = 0; V > 0; p = 0; \frac{\partial n}{\partial y} = 0$
Grounded electrodes	$u_x = u_y = u_z = 0; V = 0; n = 0; \frac{\partial p}{\partial y} = 0$
Top surface $(y = H)$	$u_x = u_y = u_z = 0; \frac{\partial T}{\partial y} = 0; \frac{\partial V}{\partial y} = 0; \frac{\partial n}{\partial y} = 0; \frac{\partial p}{\partial y} = 0$
Bottom wall $(y = 0)$	$-k_s\frac{\partial T}{\partial y} = q_w = 1 \times \frac{10^6 W}{m^2}; \frac{\partial V}{\partial y} = 0$
Inlet $(x = 0)$	$u_x = u_{in}; u_y = u_z = 0; T_f = 293.15K; \frac{\partial T_s}{\partial x} = 0; \frac{\partial V}{\partial x} = 0; \frac{\partial p}{\partial x} = 0; \frac{\partial n}{\partial x} = 0$
Outlet $(x = L)$	$\frac{\partial u}{\partial x} = 0; \frac{\partial T}{\partial x} = 0; \frac{\partial V}{\partial x} = 0; \frac{\partial p}{\partial x} = 0; \frac{\partial n}{\partial x} = 0$
Sidewalls $(z = 0, W)$	$\frac{\partial T}{\partial z} = 0; \frac{\partial V}{\partial z} = 0$

Table 2
Properties of deionized (DI) water.

Property	Value
Density $[kg/m^3]$	998.2
Thermal conductivity $[W/mK]$	0.59801
Viscosity $[kg/ms]$	$2.414 \times 10^{-5} \times 10^{\frac{247.8}{T-140}}$
Specific heat $[J/kgK]$	4185
Dielectric permittivity $[F/m]$	7.08×10^{-10}
Ionic mobility $[m^2/Vs]$	1.50×10^{-08}
Ionic diffusivity $[m^2/s]$	3.79×10^{-10}
Electric conductivity $[S/m]$	5.50×10^{-06}

Table 3
Properties of silicon.

Property	Value
Density $[kg/m^3]$	2330
Thermal conductivity $[W/mK]$	148
Specific heat $[J/kgK]$	710
Dielectric permittivity $[F/m]$	1.04×10^{-10}

D is the gap between the high and grounded electrodes. The condition $C_0 > 1$ is essential for the onset of fluid motion due to the Onsager–Wien effect [31]. For the parameter space and working fluid properties considered herein, C_0 varies from 2.3810 to 7.7431. The average friction factor f is calculated based on the pressure drop ΔP across the total channel length L as follows [47]:

$$f = \frac{2\Delta P D_H}{\rho_f L U_{av}^2} \quad (20)$$

The local heat transfer coefficient and the local Nusselt number are defined as follows [58]:

$$h(x) = \frac{q_w}{T - T_{in}} \text{ and } Nu(x) = \frac{h(x) D_H}{k_f} \quad (21)$$

The average Nusselt number is obtained as $Nu_M = \frac{1}{L}\int_{x=0}^{L} Nu(x).dx$. The performance factor, a function of both heat transfer enhancement and pressure drop penalty, is defined as follows [59]:

$$PF = \frac{Nu_{M(Re_{EL}>0)}/Nu_{M(Re_{EL}=0)}}{\left(\Delta P_{Re_{EL}>0}/\Delta P_{Re_{EL}=0}\right)^{1/3}} \quad (22)$$

3. Numerical methodology and code validation

3.1. Numerical methodology

The governing equations for flow, heat transfer, electric potential, and charge conservation are solved using the open-source software package OpenFOAM®. The electrostatic equations are incorporated into the existing finite-volume framework available in OpenFOAM®. The standard finite-volume procedures available in OpenFOAM®, as described in [60], are used to discretize the governing equations. The central differencing scheme is used to discretize the Laplacian terms, and the cubic scheme is used to discretize the gradient terms. The convection terms are discretized using the total variation diminishing (TVD) Van Leer scheme [61]. The time derivatives are discretized using an implicit Euler backward method. A PIMPLE-algorithm-based iterative procedure is used to solve the discretized equations [62]. The sparse matrices produced as a result of the discretization procedure are solved with an absolute tolerance of 1×10^{-08}.

3.2. Code validation and grid independence study

The numerical solver used to solve the fluid flow and conjugate heat transfer problem coupled with the Onsager–Wien effect-induced flow is validated by comparing with four benchmark cases. First, the numerical model of the Onsager-Wien effect used in this study is validated against the experimental and finite-element-method-(FEM)-based numerical results of Fernandes et al. [46]. The computational domain is setup to mimic the experimental conditions used in ref [46]. A parallel plate electrode configuration with a cylindrical wire electrode at the center of the domain are considered. The no-slip boundary condition is applied over all electrode surfaces. The periodic boundary condition for all variables is applied at the lateral boundaries. The wire electrode is grounded, and the high-voltage power supply is connected to the plate electrodes. A detailed description of the boundary conditions is presented in [46]. A schematic representation of the flow problem is presented in Fig. 2a. The flow structure and direction obtained in the present simulations (see Fig. 2c) are consistent with those reported by Fernandes et al. [63] (Fig. 2b). A quantitative comparison of the y-velocity profiles along the horizontal line $y = 3.75mm$ under the applied voltages 0.5, 1, and 1.5 kV are presented in Fig. 3. The numerical results obtained herein closely match with the experimental and FEM results obtained by Fernandes et al. [46]. Thus, the numerical model of EHD conduction pumping flow based on the Onsager–Wien effect used herein is validated.

The capability of the numerical model used herein to simulate the flow and conjugate heat transfer in a straight microchannel is tested by comparing the results obtained in this study with the correlations of Phillips et al. [63] and Steinke and Kandlikar [64]. The Nusselt number distribution along the center line in the bottom of the channel is compared with the correlation of Phillips et al. [63], as illustrated in Fig. 4a. The operating conditions applied in this validation case are presented in the inset figure of Fig. 4a. The average friction factor at different Reynolds numbers in the laminar regime obtained in the numerical simulations conducted herein are compared to the correlation of Steinke and Kandlikar [64], as shown in Fig. 4b. The numerical simulation results of this study agree well with the benchmark results.

The numerical model presented herein solves for the electric potential distribution in both the solid and liquid regions in a coupled manner. It is necessary to ensure that the electric potential coupling between the solid and liquid regions is smooth, without any non-physical oscillations across the interface. To verify the electric potential coupling across the solid–liquid regions, a validation case is setup with a one-dimensional (1D) domain consisting of three layers (Solid 1, Fluid 1, and Fluid 2). All three layers possess different electrical permittivity, as depicted in Fig. 5a. The numerical model presented herein is able to ensure smooth transition of electric potential across the three layers. The comparison of electric potential profile across the layers obtained herein is compared to the solution provided by Roghair et al. [65]. The electric potential profile obtained herein exhibits smooth transitions across the three layers (see Fig. 5b), and is in good agreement with the benchmark result.

A structured, orthogonal grid with fine cells in the fluid region is employed in this study. The grid resolution used in this study is decided based on the results of a grid sensitivity analysis, which are presented in Table 4. Three grids A, B, and C consisting of 2,614,000, 4,114,000, and 5,614,000 cells were considered. The average velocity U_{av}, maximum velocity U_{max}, average temperature T_{av}, maximum temperature T_{max}, pressure drop ΔP, and mean Nusselt number Nu_M values obtained using the three aforementioned grids are compared to each other. The variation between grids B and C is less than 3 % for all parameters. Thus, grid B (shown in Fig. 6) is chosen for all of the simulations presented in this study.

In general, for the range of Reynolds number considered in this study, the flow is laminar and steady. However, it is necessary to check for any unsteadiness in the flow induced by the Onsager–Wien effect. Thus, all of the simulations performed herein are transient in nature. The adaptive time stepping method has been adopted with the maximum Courant number = 0.5. Thus, in all of the simulations, the time step size

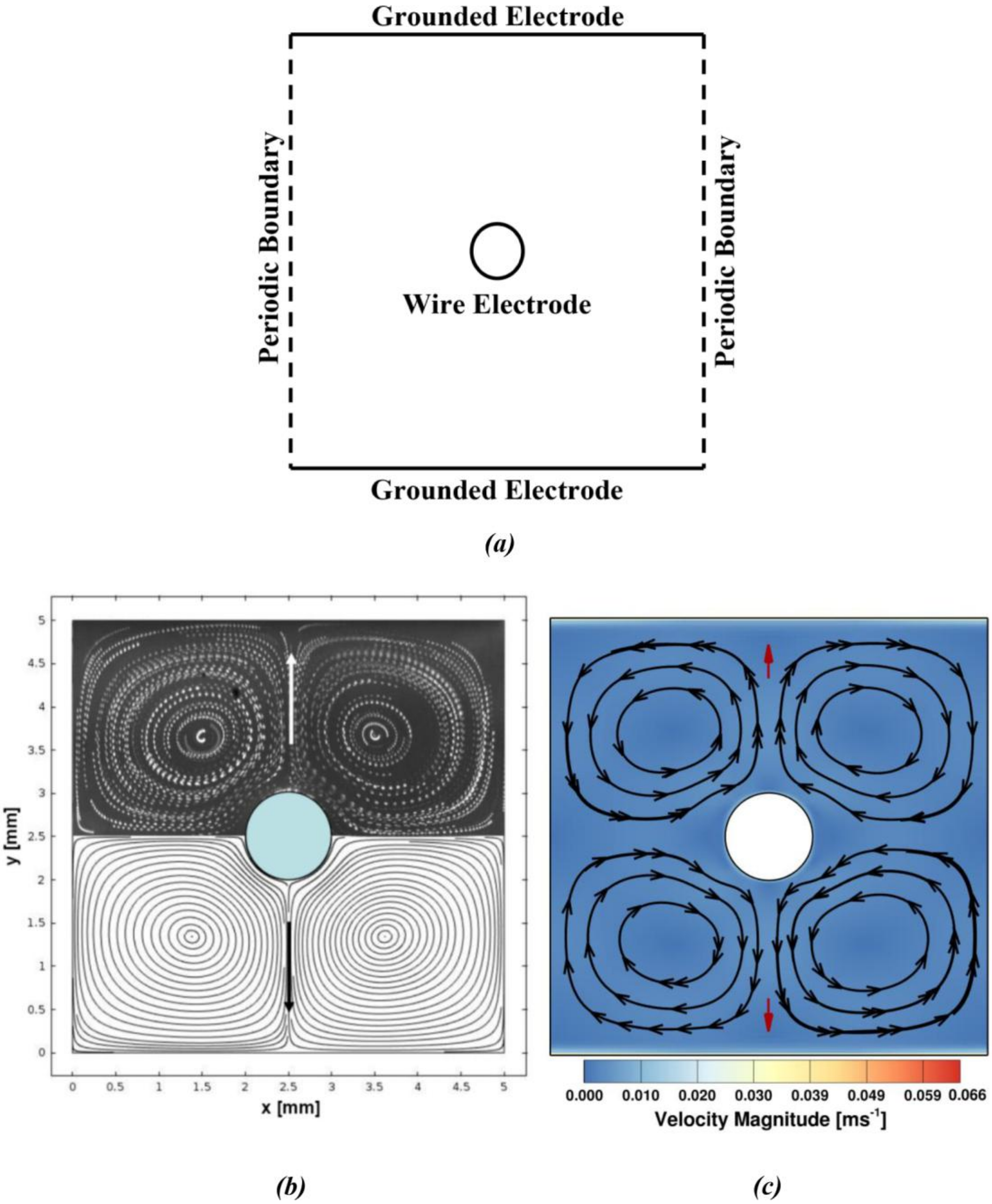

Fig. 2. Comparison of flow pattern obtained in the present numerical simulations with the experimental and finite-element-method-based numerical results of Fernandes et al. [46]. (a) Schematic representation of the flow domain, (b) Experimental (top half) and numerical (bottom half) flow pattern reported in ref [46], and (c) Flow pattern obtained in the present numerical simulations.

based on the above maximum Courant number criterion varied in the range of 1×10^{-7} to $1 \times 10^{-6} s$. This is an adequately small-time step for capturing any unsteadiness in such simulations. However, even in the presence of the Onsager–Wien effect, the flow exhibited a laminar steady state. The time evolution of the magnitude of mean velocity in the fluid region and mean temperature in the entire computational domain is plotted in Fig. 7. Both the velocity and temperature reached steady states even at the highest values of Re and Re_{EL} considered in this study. Although the flow pattern and vortices in the cases with $Re_{EL} > 0$ appears chaotic, the flow exhibits a steady state. Thus, all of the results presented herein represent steady state values at $t = 0.1s$.

4. Results and discussion

Developing laminar flow and conjugate heat transfer in a 3D straight rectangular microchannel in the presence of electric-field-induced Onsager–Wien effect are studied. The morphology of the flow vortices induced by the Onsager–Wien effect is presented. The driving parameter for the inlet channel flow is the Reynolds number Re and is varied in the range of $250 \leq Re \leq 1000$. The parameter that quantifies the EHD flow vortices generated by Onsager-Wien effect is the electric Reynolds number Re_{EL}. The electric Reynolds number is varied at four levels 0, 5, 10 and 15, respectively. The boundary layer disruption caused by the EHD vortices is explained. Finally, the hydraulic and thermal performance of the microchannel, at different levels of Re and Re_{EL} are evaluated.

4.1. Vortices induced by the Onsager–Wien effect

Firstly, it is important to understand the morphology of the flow

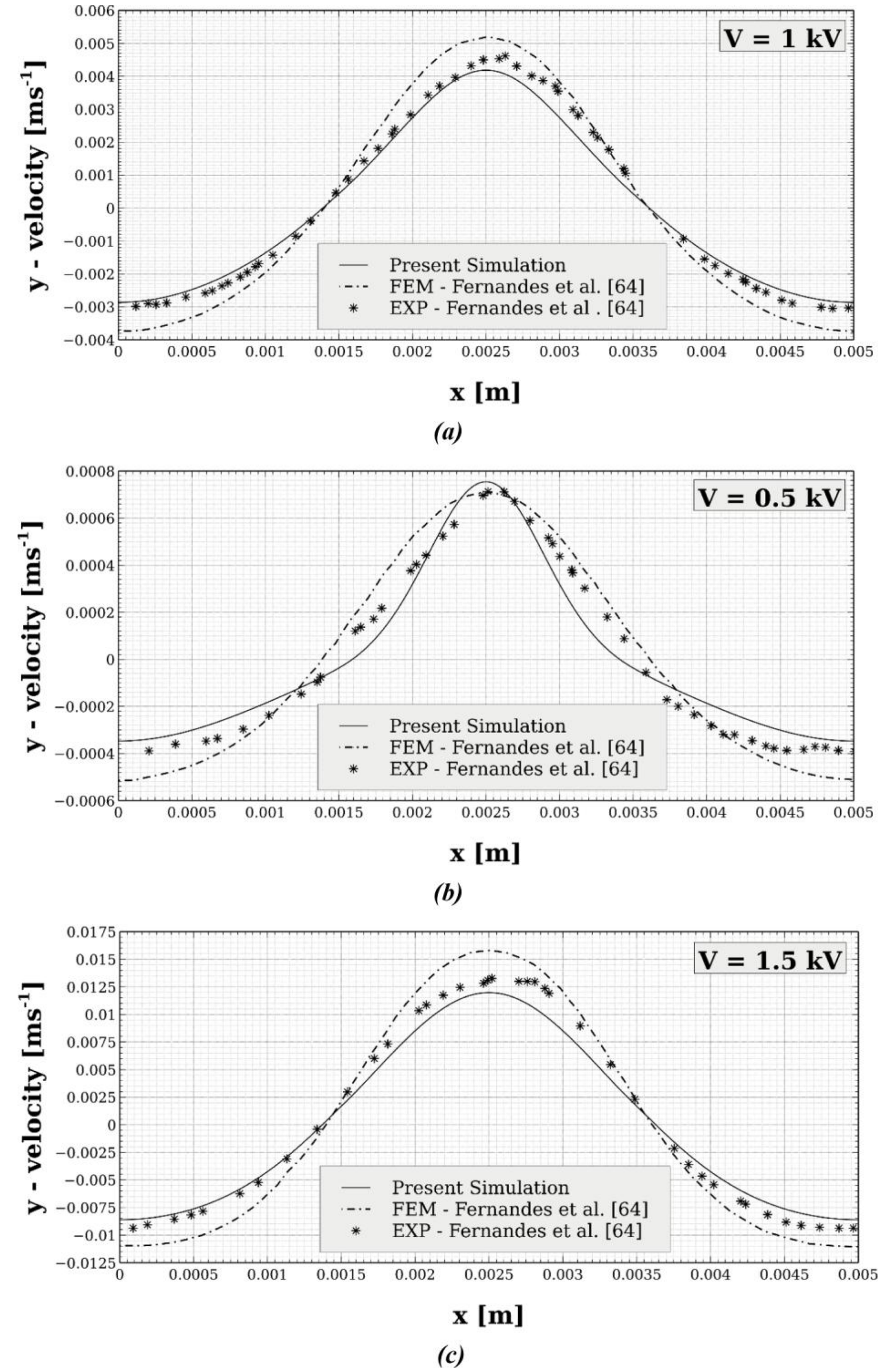

Fig. 3. Comparison of y–velocity profile along $y = 0.35\,mm$ obtained by present simulations with experimental and numerical results of Fernandes et al. [46].

vortices induced purely by the Onsager–Wien effect. To this end, a case without any external flow ($Re = 0$) and heat flux ($q_w = 0$), but with electric field $Re_{EL} = 5$, 10, and 15, are considered. Thus, the flow field in the microchannel is governed purely by the Onsager–Wien effect. The zoomed view of velocity distribution and vectors in the region from electrode pair 2 to 3 (at $Re = 0$, $q_w = 0$, and $Re_{EL} = 15$) is shown in Fig. 8. It is seen that the flow vortices start from the smaller high voltage electrode and are directed towards the wider low voltage electrode. The flow velocity is also intense near the shorter high voltage electrode, as compared to the velocity distribution in the proximity of wider grounded electrodes. This observation matches well with the EHD conduction flow phenomenon reported in ref. [66]. This phenomenon can be attributed to the asymmetricity in the size of high and grounded electrodes. The wider grounded electrodes can hold more positive charges as compared to the quantity of the negative charges which the shorter high voltage electrodes can hold. Thus, there are more free negative charges that are let loose from the negative hetero-charge layer above the smaller high voltage electrodes. These free negative charges migrate towards the positive hetero-charge layer formed over the wider grounded electrodes. This movement of free charges from the shorter electrode towards the wider electrode explains the flow vortices directed from the shorter to wider electrodes. It is to be noted that these flow

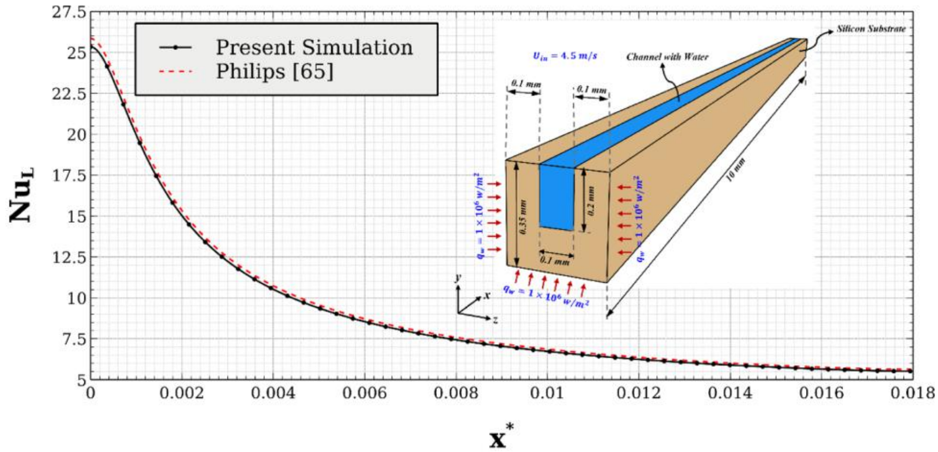

(a)

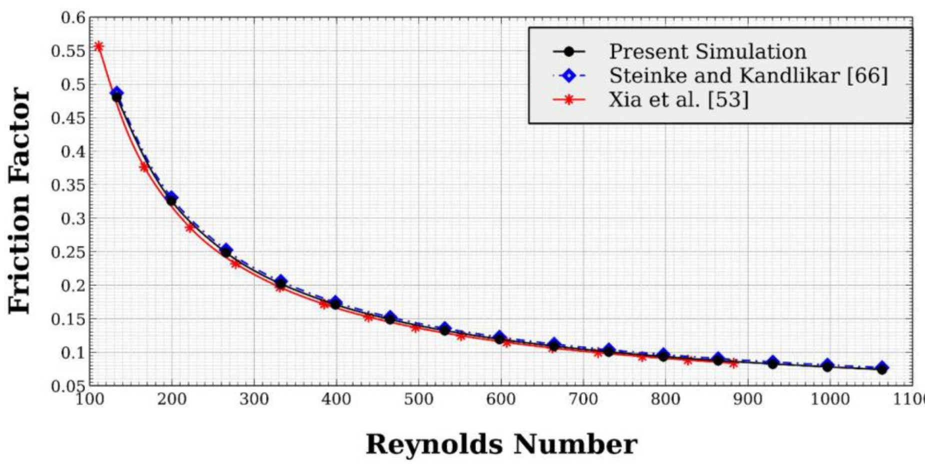

(b)

Fig. 4. Comparison of (a) Local Nusselt number along the bottom wall of the channel with the correlation of Phillips et al. [63] and (b) Friction factor with correlation of Steinke and Kandlikar [64] and numerical results of Xia et al. [47].

vortices due to electric field are local to the region close to the electrodes flushed in the bottom wall of the channel. The velocity distribution is zero in the regions away from the electrode. Sharp variations in velocity are observed close to the electrodes. Especially, the peak velocities are noted close to the shorter high-voltage electrodes. The velocity vectors indicate the formation of rotating vortices above the electrodes.

The peak and average velocities in the microchannel at $Re = 0$, $q_w = 0$, and $Re_{EL} = 5$, 10 and 15 are presented in Table 5. Both the average and peak velocities vary as a function of electric Reynolds number Re_{EL}. However, the increase in average velocity U_{av} is very marginal with respect to the increase in Re_{av}. This observation confirms that the EHD generated vortices are local to the region close to the electrodes and their influence on the main channel flow is minimal. In contrast to the marginal increase of U_{av} with respect to increase in Re_{EL}, the maximum velocity U_{max} in the domain is a strong function of electric Reynolds number Re_{EL}. The values of U_{max} correspond to the sharp high velocity distributions observed in the region close to the shorter high voltage electrodes (see Fig. 8). The peak velocity values notably increase with the increase of Re_{EL}. This indicates that the net flow field is minimally affected by the Onsager–Wien effect. By contrast, the local velocity distribution close to the electrodes are significantly enhanced by the Onsager–Wien effect. In other words, in the region close to the electrodes, the Onsager–Wien effect produces small vortices with a localized high-velocity gradients.

The vortex structures generated purely by the Onsager–Wien effect at $Re_{EL} = 5$, 10, and 15 are presented in Fig. 9. The vortex structures generated by the Onsager-Wien effect are clearly seen. Corresponding to each electrode pair vertical vortex structures with stronger velocity distributions are noted near the smaller high voltage electrodes. Whereas, the vortices near the grounded electrode are wider and have comparatively weak velocity distribution. It is to be noted that the vortex structures become more prominent with increasing values of electric Reynolds numbers Re_{EL}. The velocity magnitudes of the vortex structures are also notably higher at higher values of electric Reynolds numbers. The vortices are thin and with lower velocity distribution at $Re_{EL} = 5$. The maximum velocity value is approximately close to 2.2 ms^{-1}. Whereas, the vorticity structures are much wider at $Re_{EL} = 15$ and the peak velocity in the vortex structures is around $4.8ms^{-1}$. These vortices are similar to the vortices generated by roughness on the microchannel wall [57,59]. Thus, it can be inferred that the Onsager–Wien effect introduces a pseudo-roughness effect in the microchannel.

4.2. Boundary layer disruption due to pseudo-roughness effect

Following the explanation of the vortex structure generated purely by Onsager-Wien effect in Section 4.1, we move forward to explore the combined interaction of EHD generated vortices with the main inlet channel flow in the presence of applied heat flux. For the Re values considered herein, the flow is in laminar and steady regime. The velocity

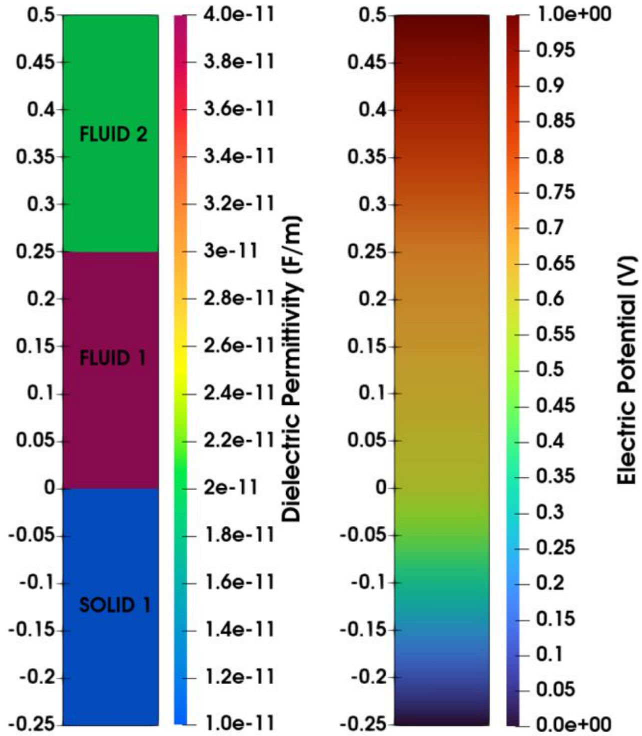

(a)

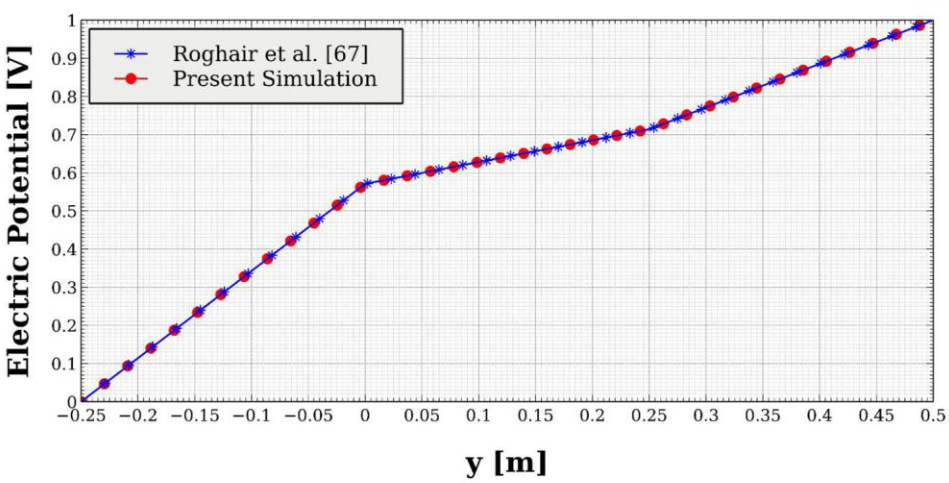

(b)

Fig. 5. (a) Schematic of the three layers (Solid 1, Fluid 1, and Fluid 2) with discontinuities in dielectric permittivity and electric potential distribution. (b) Electric potential distribution along a vertical line across the three layers compared to that reported by Roghair et al. [65].

contours of the base flow at $250 \leq Re \leq 1000$ and those in the absence of the electric field ($Re_{EL} = 0$) are depicted in rows 1–4 of Fig. 10. The flow is evidently laminar, and the laminar boundary layer is prominent. The velocity magnitude distribution gets higher as the Reynolds number is increased from 250 to1000. In the absence of electric field effects, the flow is perfectly smooth without any disturbances. The laminar boundary layer prevents fluid mixing and, thus, limits heat transfer from the bottom wall. Corresponding to the smooth laminar flow observed in the absence of electric field, smooth thermal boundary layer at $250 \leq Re \leq 1000$ and $Re_{EL} = 0$ is noted in the temperature contours presented in rows 1–4 of Fig. 11. At $Re = 250$, the thermal boundary layer is very thick and with high temperature distribution. The thermal boundary layer is seen developing from the entrance region and then gets thicker along the length of the channel. It is also to be noted that the thermal boundary layer gets thinners as the flow Reynolds number is increased from 250 to 1000. But, even at the highest values of Reynolds number ($Re = 1000$), a well-defined, smooth thermal boundary is clearly noticed.

The flow morphology in the presence of electric field induced vortices at $250 \leq Re \leq 1000$ and $Re_{EL} = 15$ are presented in rows 5–8 in Fig. 10. The laminar boundary layer (as noted in rows 1–4 of Fig. 10) is evidently disrupted by the EHD conduction induced vortices (see rows 5-8 of Fig. 10). Notably, the vortices induced by the Onsager–Wien effect has disrupted the viscous boundary layer, and fluid mixing is evident. The boundary layer disruption is stronger at higher Reynolds numbers, indicating that the pseudo-roughness induced by the Onsager-Wien effect is minimum in the viscous-dominated flows at $Re = 250$. By contrast, the inertial flow at higher values of Re favors the boundary

Table 4
Results of grid sensitivity analysis.

Grid	$U_{av}[m/s]$	% Diff	$U_{max}[m/s]$	% Diff	$T_{av}[K]$	% Diff	$T_{max}[K]$	% Diff	$\Delta P[kPa]$	% Diff	Nu_M	% Diff
$Re = 250$ and $Re_{EL} = 0$												
A	1.459	–	3.4781	–	322.01	–	331.46	–	34.21	–	7.4336	–
B	1.557	6.71	3.6444	4.78	326.59	1.42	339.54	2.44	34.39	0.53	7.5087	1.01
C	1.601	2.82	3.6512	0.19	326.94	0.11	340.59	0.31	34.40	0.02	7.5112	0.03
$Re = 1000$ and $Re_{EL} = 0$												
A	5.673	–	13.886	–	310.22	–	315.41	–	16.21	–	20.623	–
B	6.202	9.32	14.398	3.69	311.92	0.55	319.57	1.32	16.28	0.48	20.855	1.12
C	6.294	1.48	14.562	1.14	312.11	0.06	320.21	0.20	16.31	0.16	20.913	0.28
$Re = 250$ and $Re_{EL} = 15$												
A	1.112	–	7.1123	–	316.73	–	330.59	–	91.02	–	8.992	–
B	1.642	4.77	7.4094	4.17	322.88	1.94	336.39	1.75	91.18	0.17	9.254	2.91
C	1.678	2.19	7.5132	1.40	324.41	0.47	337.01	0.18	91.23	0.06	9.354	1.08
$Re = 1000$ and $Re_{EL} = 15$												
A	5.823	–	20.111	–	299.32	–	301.51	–	308.11	–	20.035	–
B	6.206	6.58	20.451	1.69	304.74	1.81	308.64	2.36	309.03	0.30	21.453	7.08
C	6.339	2.14	20.623	0.84	306.52	0.58	309.93	0.42	309.94	0.31	21.947	2.30

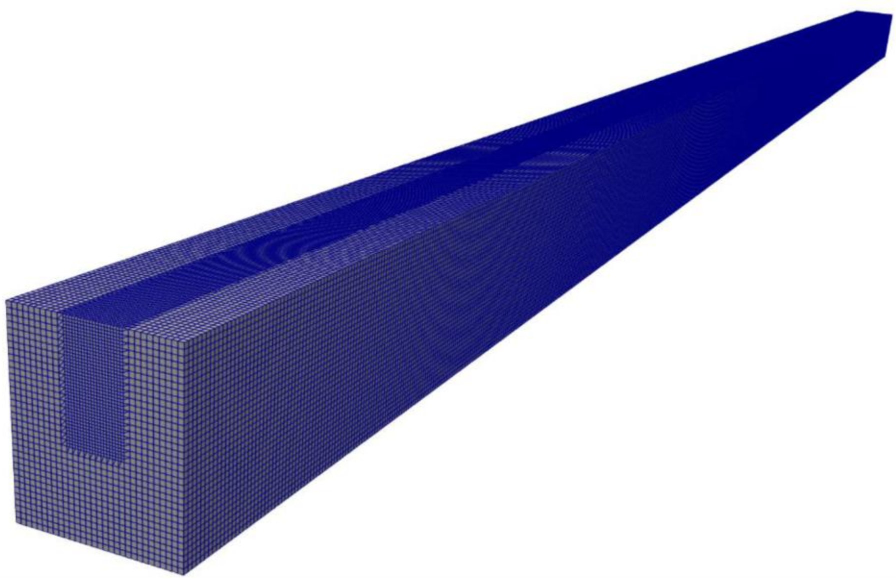

Fig. 6. Mesh used in this study.

layer disruption due to the pseudo-roughness induced by the Onsager–Wien effect. Corresponding to the viscous boundary layer depletion explained with reference to contours in rows 5–8 of Fig. 10, the thermal boundary layer disruption by the Onsager-Wien effect induced vortices is presented in rows 5–8 of Fig. 11. In contrast to the smooth thermal boundary layers reported in the absence of electric field ($Re_{EL} = 0$) in rows 1–4 of Fig. 11, the thermal boundary layers in rows 5–8 of Fig. 11 is not smooth. At $Re = 250$ and $Re_{EL} = 15$, the thermal boundary layer is not smooth as compared to the case without electric field ($Re = 250$ and $Re_{EL} = 0$). The thermal layer boundary depletion effect is more prominent in the developing region of the thermal boundary layer. However, in the fully developed region, the viscous forces begin to dominate and the thermal boundary layer suppression is suppressed. At higher values of Reynolds number ($Re > 250$), the viscous forces are weak and the inertial forces are strong. This favors the action of EHD generated vortices and the resultant thermal boundary layer depletion is evidently visible.

A 3D view of the vortex structures produced by the Onsager–Wien effect at $250 \leq Re \leq 1000$ and $Re_{EL} = 15$ is presented in Fig. 12. The vortices are small and discontinuous at $Re = 250$. The EHD generated vortices are more local to the high voltage electrodes but, the vortices near the grounded electrodes are weak and are less prominent. The vortices near the wider high voltage are too weak to deplete the strong viscous boundary layer observed at low Reynolds number value of $Re = 250$. As explained in the contours of temperature, this proves the weakness of EHD vortices at strong viscous flow observed at lower value of flow Reynolds number. At higher values of flow Reynolds number, the viscous effects are minimized. Furthermore, the main inlet flow in the channel is in the positive $x-$ direction. Thus, the inertial flow direction favors the EHD vortices that are also directed towards the positive $x-$ direction. As a result, the EHD vortices get more spread and continuous along the lenght of the microchannel. Especially, the weak vortices over the wide grounded electrodes also get prominent with increasing values of flow Reynolds number. From these findings, it can be inferred that the vortices induced by the Onsager–Wien effect introduced vortices produce a pseudo-roughness and effectively disrupt the viscous and thermal boundary layers.

4.3. Flow and heat transfer performance evaluation

The effects of the flow vortices induced by the Onsager–Wien effect on the flow and heat transfer characteristics are elaborated in this section. The average and maximum velocities in the fluid region at $250 \leq Re \leq 1000$ and $5 \leq Re_{EL} \leq 15$ are presented in Fig. 13. Similar to the observation made in the case with pure EHD conduction governed flow (see Table 5), the mean velocity in the microchannel is more or less

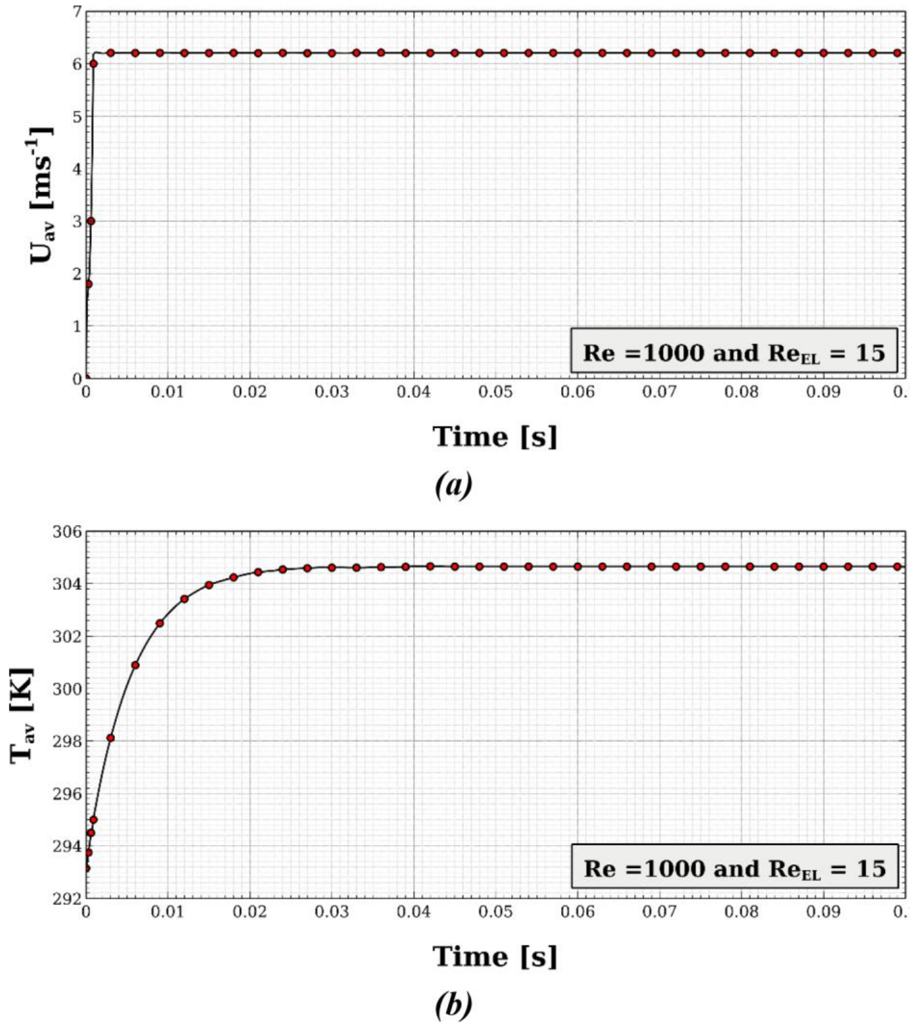

Fig. 7. Time evolution of (a) Mean velocity in the fluid domain and (b) Mean temperature in the entire computational domain at $Re = 1000$, $Re_{EL} = 15$, and.$q_w = 1 \times 10^6\ W/m^2$.

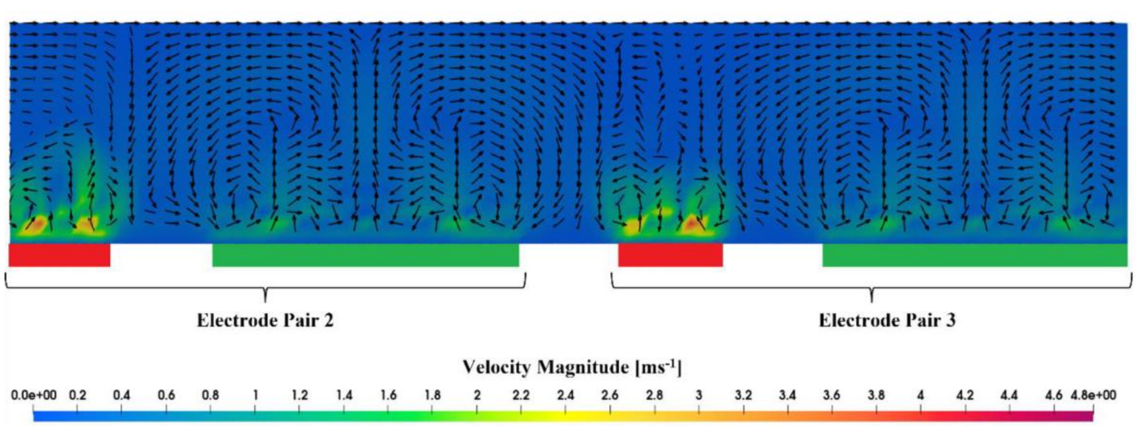

Fig. 8. Velocity field in the region from EP2 to EP3 at $Re = 0$ and $Re_{EL} = 15$ under isothermal conditions.

unaffected by the presence electric field (refer to Fig. 13a). Even in the presence of main channel flow and applied heat flux, the average velocity in the microchannel is only a function of flow Reynolds number Re. The average velocity values are unaffected by the value of electric Reynolds number Re_{EL}. Thus, it is confirmed that the EHD vortex generation is a phenomenon that is local to the region in the proximity of electrodes. Contrary to the values of mean velocity, the maximum velocity values strongly depend on the values of Re_{EL}, as seen in Fig. 13b. This can be attributed to the sharp gradients in velocity observed in the EHD generated vortices. As seen in Figs. 8 and 9, the EHD vortices gets stronger with increase in Re_{EL}. These sharp velocity gradients within the vortices induced by the Onsager–Wien effect account for the maximum

Table 5
Mean and maximum velocities in the domain at $Re = 0$ and $q_w = 0\,W/m^2$.

Re_{EL}	$U_{av}[m/s]$	$U_{max}[m/s]$
5	0.1026	2.2230
10	0.1319	3.7362
15	0.1867	4.7765

velocities in the fluid domain. The maximum velocity observed in the fluid domain is higher at higher *Re*. Moreover, stronger electric fields are capable of generating stronger vortices with higher velocity distributions. The increase in maximum velocity with the increase of electric Reynolds number Re_{EL} is minimum at $Re = 250$. The dominant role of the thick viscous boundary layer at low Reynolds number is attributed to this observation. With the increase of flow Reynolds number to intermediate values, the viscous effects are minimized and inertial forces begin to dominate the flow. As explained in Fig. 9, the inertial forces favor the EHD vortices and thus, the increase in maximum velocity with respect to the increase in Re_{EL} is more evident at $Re = 500$ and 750. At $Re = 1000$, again, the difference in maximum velocities between the cases with and without an electric field begins to decrease. The inertial effect of the base flow becomes too strong as compared to the EHD-induced vortices. The base velocity imparted by the inlet flow is already higher and becomes comparable to the sharp velocities in the EHD vortices. Thus, the effect of Re_{EL} on U_{max} begins to diminish at $Re = 1000$.

The difference in mean temperature (ΔT) between the solid and liquid regions indicate the effectiveness of convective heat transfer by the fluid flow. Higher values of ΔT indicate that less heat is transported by the liquid flow. The variation of ΔT with respect to $250 \leq Re \leq 1000$ and $5 \leq Re_{EL} \leq 15$ is plotted in Fig. 14a. In general, ΔT tend to decrease as *Re* and Re_{EL} increased. This indicates that higher *Re* and Re_{EL} values improve the heat transfer between the solid and liquid. At $Re = 250$, ΔT values are higher due to the poor heat transfer limited by the viscous

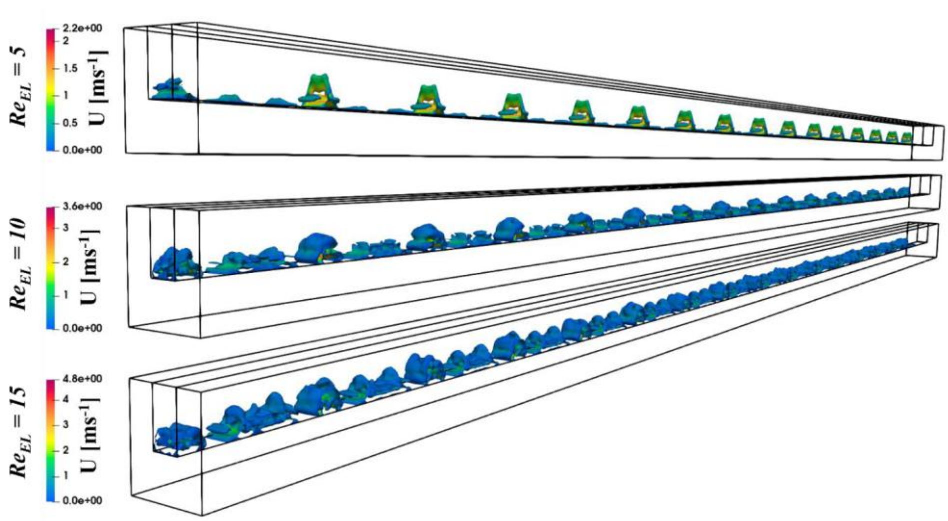

Fig. 9. Vortex structure generated by the Onsager-Wien effect in the absence of external flow and heat flux. Row – 1: $Re_{EL} = 5$, Row – 2: $Re_{EL} = 10$ and Row – 3: $Re_{EL} = 15$.

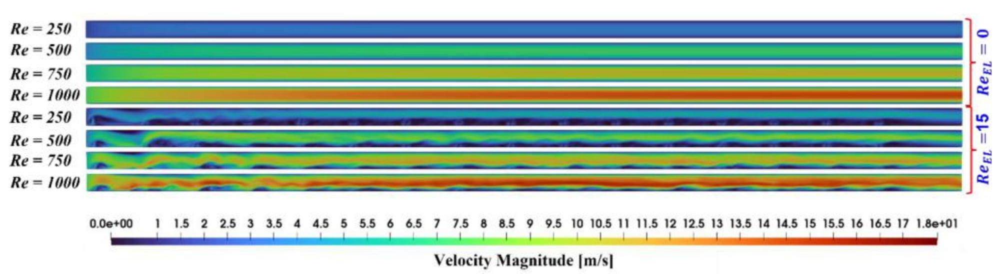

Fig. 10. Velocity field at $250 \leq Re \leq 1000$, electric Reynolds number $Re_{EL} = 0$ and 15 and heat flux.$q_w = 1 \times 10^6 W/m^2$.

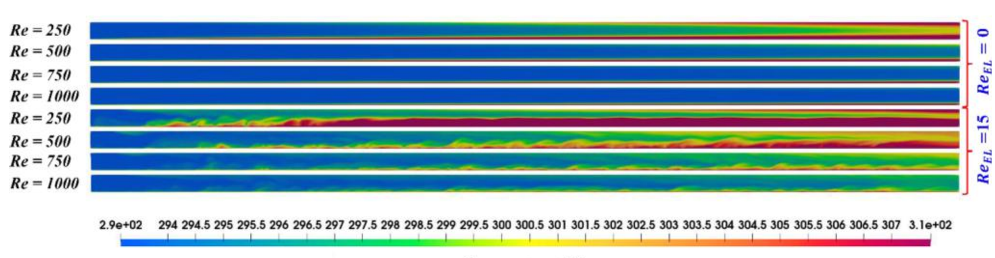

Fig. 11. Temperature field at $250 \leq Re \leq 1000$, electric Reynolds number $Re_{EL} = 0$ and 15 and heat flux.$q_w = 1 \times 10^6 W/m^2$.

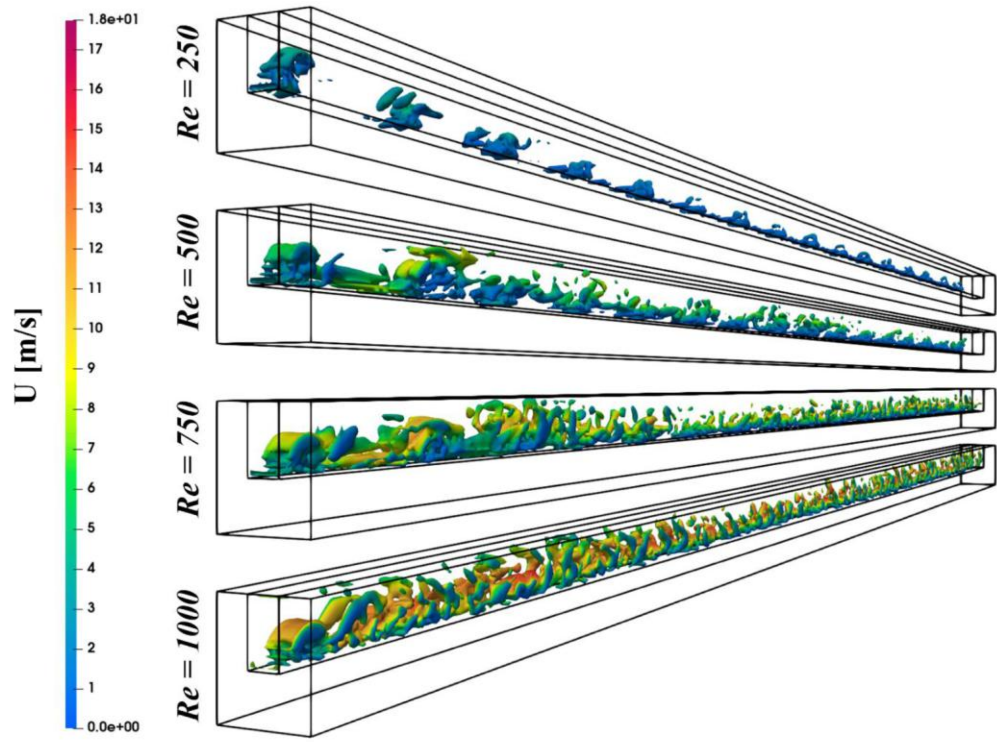

Fig. 12. Vortex structure generated by the Onsager-Wien effect in the presence of external flow ($250 \le Re \le 1000$), electric Reynolds number $Re_{EL} = 15$ and heat flux.$q_w = 1 \times 10^6 W/m^2$.

force dominated flow. At this value of flow Reynolds number, the drop in ΔT due to the increase in Re_{EL} is less. This confirms the suppression of EHD vortices by the thick viscous boundary layer flow. At $Re > 250$, ΔT drops with the increase of Re and also drops notably with increase of Re_{EL}, at any given value of Re. In addition to the variation of ΔT, variation of maximum temperature (T_{max}) in the computational domain (both solid and liquid regions) at $250 \le Re \le 1000$ and $5 \le Re_{EL} \le 15$ is presented in Fig. 14b. Synonymous to the variations seen in ΔT, T_{max} is also a function of both flow and electric Reynolds numbers. Irrespective of the value of Re_{EL}, maximum temperature values are high at $Re = 250$. This indicates the limited heat transfer observed in a smooth laminar low Reynolds number flow. Increasing the flow Reynolds number leads to thinning of thermal boundary layer and better heat transfer. Thus, T_{max} decreases with increasing values of Re. At any given value of Re, the maximum value of temperature gets lower at higher values of Re_{EL}. This observation confirms that the EHD generated vortices result in improved heat transfer. However, effect of Re_{EL} is minimum at $Re = 250$ and increases at intermediate values of Reynolds numbers ($Re = 500$ and 750). At $Re = 1000$, the effect of Re_{EL} on T_{max} again begins to decrease, due to the fact that the sharp velocity gradients brought about by the EHD vortex generation becomes less significant as compared to the main velocity field set by the higher flow Reynolds number.

The net heat transfer is expressed in terms of the mean Nusselt number. In general, the mean Nusselt number increases as the flow Reynolds number increases. The introduction of pseudo-roughness due to the Onsager–Wien effect further intensifies the heat transfer. The variation of mean Nusselt number Nu_M with respect to flow and electric Reynolds numbers is presented in Fig. 15a. Nu_M in the presence of the electric field ($Re_{EL} > 0$) is higher than that case without the electric field ($Re_{EL} = 0$), for any given value of the flow Reynolds number Re. However, the influence of Re_{EL} is suppressed by the strong viscous flow at $Re = 250$. At intermediate Reynolds numbers ($Re = 500$ and 750), the inertial flow favors the EHD generated vortices and the increase in Nu_M with increase of electric Reynolds numbers is significant. Finally, at $Re = 1000$, the inertial flow becomes much stronger to diminish the effect of EHD vortices. Thus, the increase in mean Nusselt number with respect to electric Reynolds number begins to fall.

The heat transfer enhancement due to the pseudo-roughness effect can be well understood from the local Nusselt number distribution along the center line ($z = 0.15mm$) of the bottom wall ($y = 0.15mm$) of the fluid passage. The local Nusselt number distribution at $Re = 1000$ and $0 \le Re_{EL} \le 15$ is presented in Fig. 15b. In general, the local Nusselt number distribution is higher in the entrance region, and it gradually decreases along the channel length, as the thermal boundary layer thickens along the length. The local Nusselt number distribution in the case without the electric field $Re_{EL} = 0$ is smooth along the entire channel length. By contrast, at $Re_{EL} > 0$, the local Nusselt number distribution exhibits ups and downs along the entire channel length. The ups and downs observed in the local Nusselt number profile correspond to the EHD generated vortices. Furthermore, the local Nusselt number distribution along the entire channel length is higher for higher values of electric Reynolds numbers. This clearly indicates the improvement in heat transfer because of the pseudo-roughness induced by the Onsager–Wien effect. The effect of Re_{EL} is lesser in the entrance region where the viscous effects dominate the flow. Within the developed flow region, the EHD vortices result in notable augmentation of heat transfer, leading to higher local Nusselt number distribution.

Present work employs thin and flat electrodes flushed to the bottom wall of the channel. Thus, the geometrical drag caused by the electrodes to the main inlet channel flow is negligible. However, the EHD vortices emanating from the electrode surfaces are in perpendicular direction to the inlet flow, which leads to additional pressure drop. Thus, the improvement in heat transfer because of the pseudo-roughness effect was found to be accompanied by an additional pressure drop. The variation of pressure drop across the channel length with respect to Re and Re_{EL} is depicted in Fig. 16. As expected, the pressure drop increases as the flow Reynolds number increases. However, the pressure drop increases with Re_{EL} as well, for any given Reynolds number. At $Re = 250$, the increase in pressure drop with respect to the increase in electric Reynolds number is minimal. At this value of Reynolds number, the EHD

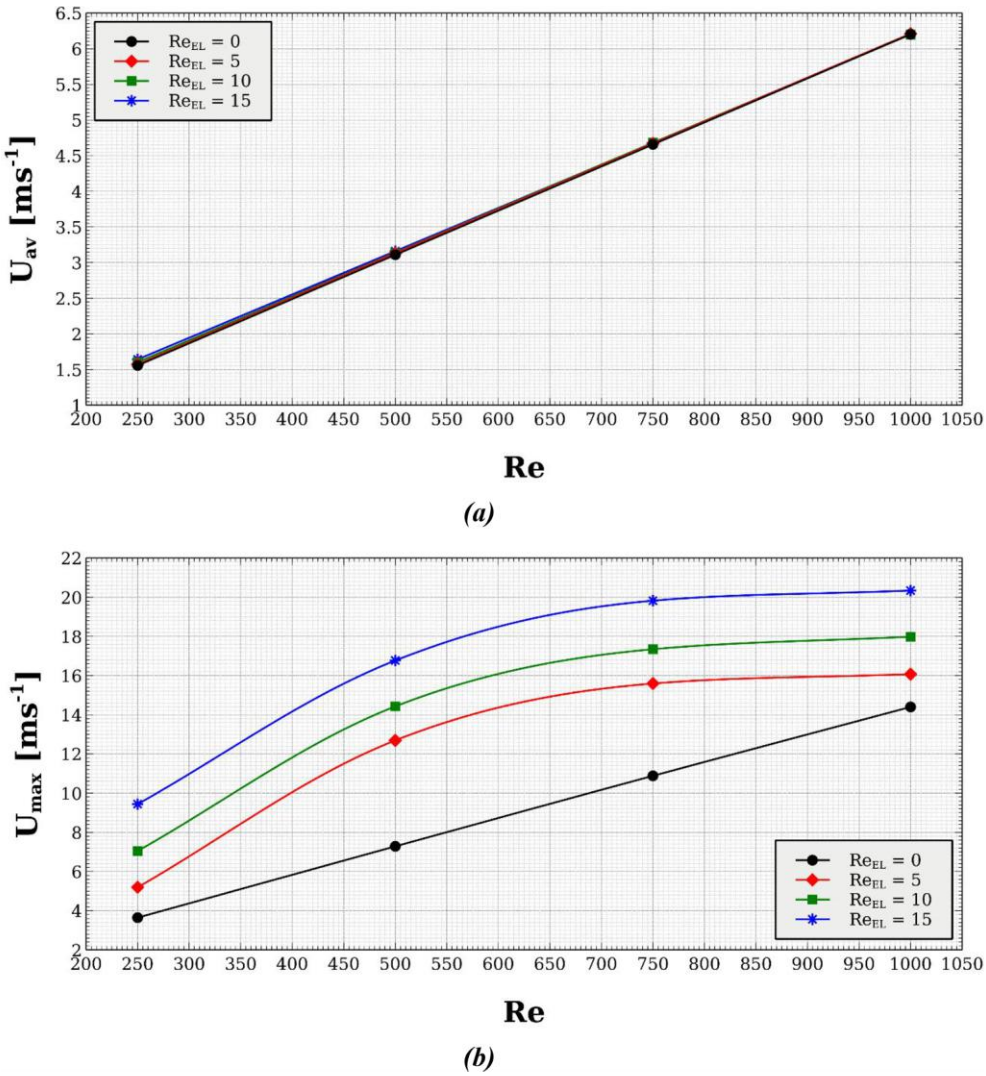

Fig. 13. (a) Average velocity and (b) Maximum velocity in the liquid region at $250 \leq Re \leq 1000$ and.$0 \leq Re_{EL} \leq 15$.

vortices are suppressed due to the strong viscous forces. Thus, the influence of electric Reynolds number on pressure drop is weak. At higher values of Reynolds number, the EHD vortices are prominent and thus, the increase in pressure drop with respect to electric Reynolds number is comparatively more significant. The performance factor *PF*, which is defined in terms of heat transfer enhancement and pressure drop, is used to evaluate the net thermo-hydraulic performance of the microchannel [59]. When the *PF* is greater than 1, the heat transfer enhancement due to the Onsager–Wien effect is higher than the incurred penalty in pressure drop. By contrast, when $PF < 1$, the pressure drop penalty is higher than the achieved increase in heat transfer. The performance factor *(PF)* at different combinations of electric Reynolds number *(Re_{EL})* and Reynolds number *(Re)* are presented in Fig. 17. At $Re = 250$ and $Re_{EL} = 5$, the value of *PF* is approximately equal to 1. This indicates that the increase in heat transfer and the accompanying increase in pressure drop are equal and no real benefit is achieved by the generation of EHD vortices. At $Re = 250$ and $Re_{EL} > 5$, the pumping power loss incurred is greater than the obtained heat transfer. Thus, the performance factor falls below 1 at $Re = 250$ and $Re_{EL} > 5$. In the viscous dominated flow observed at $Re = 250$, the performance factor decreases with increase in Re_{EL}. As the flow shifts to inertia dominated regime at higher values of *Re*, a shift in trend is observed. In the inertia dominated regime ($Re > 250$), the performance increases with the increases in electric Reynolds numbers. Furthermore, in this regime, the value of *PF* is greater than 1 for all combination of *Re* and Re_{EL}. This observation aligns with the fact that the inertial flow favors the action of EHD vortices. A maximum of $PF = 1.26$ is recorded at the flow Reynolds number $Re = 1000$ and electric Reynolds number $Re_{EL} = 15$.

The electric power consumed to induce the Onsager–Wien effect is calculated as $P_{EL} = V \times I_{tot}$, where *I* denotes the electric current flowing from the high-voltage electrodes to the grounded electrodes. The total electric current is computed by integrating the net current density flux $\overrightarrow{J}$ over the surface of all the high-voltage electrodes as follows [66]:

$$I_{tot} = \iint \overrightarrow{J}.\widehat{n} dS \tag{23}$$

where,

$$\overrightarrow{J} = \frac{\partial \varepsilon_f \overrightarrow{E}}{\partial t} + (Kp + Kn)\overrightarrow{E} + (p - n)\overrightarrow{u} - (D\nabla p - D\nabla n) \tag{24}$$

The time averaged (over a period of 0.1 *s*) values of electric current and power consumption at different values of *Re* and Re_{EL} are listed in Table 6. The maximum electric power consumption is 8.8671 *mW* at $Re = 1000$ and $Re_{EL} = 15$. In that specific case, the mean Nusselt number increased by 56.04 % with an additional electric power consumption of just a few milliwatts. Results of the present study indicate that generating EHD vortices by Onsager-Wien effect is a potential and economically viable approach to enhance heat transfer in a

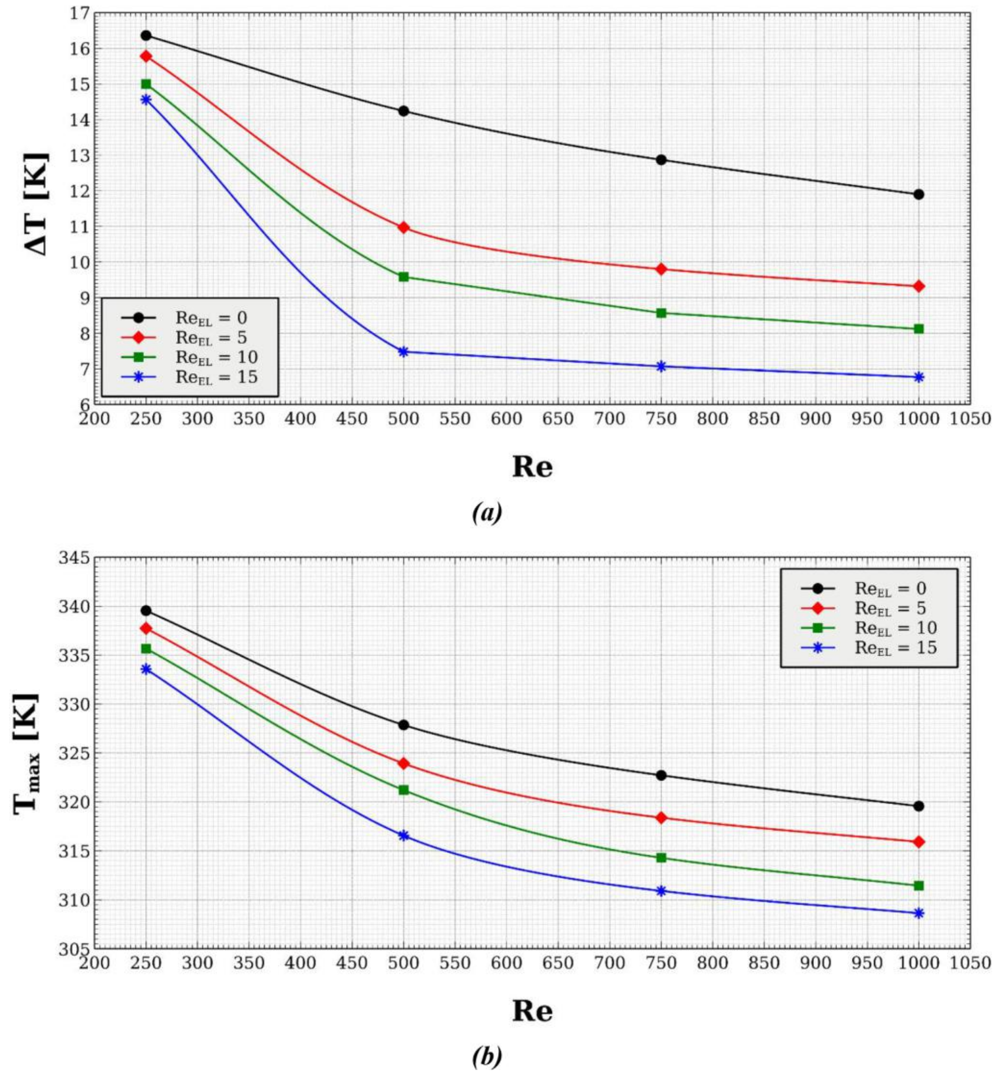

Fig. 14. (a) Difference between the mean temperature in the solid and liquid regions, and (b) Maximum temperature in the entire whole computational domain at $250 \leq Re \leq 1000$ and $0 \leq Re_{EL} \leq 15$.

microchannel.

5. Concluding remarks

In this work, a 3D numerical investigation of the flow and conjugate heat transfer in a straight rectangular microchannel is presented. The pseudo-roughness induced by the Onsager–Wien effect owing to the electric-field-enhanced dissociation of ions is considered. Unlike the previous studies on EHD conduction pumping flow-based heat transfer enhancement, this study proposed a novel design to deplete the thermal boundary layer by Onsager-Wien effect induced vortices. The proposed design operates at weak/medium electric fields at low applied voltages, thus, leading to safe operation and low power consumption. The mechanism of boundary layer disruption by EHD generated vortices and the resulting enhancement in heat transfer at different flow Reynolds numbers *Re* and electric Reynolds numbers Re_{EL} are investigated. The main conclusions of this study based on an analysis of the results are as follows:

1) The electrode pairs flushed on to the bottom of the channel generates small vortices due to Onsager–Wien effect. These vortices due to Onsager-Wien effect exhibit localized high velocities close to the bottom wall.
2) The viscous and thermal boundary layers are effectively disrupted by the EHD-induced vortices. The heat transfer at the bottom wall and the mean Nusselt number is enhanced by the Onsager–Wien effect.
3) The effect of the vortices is minimal on the viscous-force-dominated flow at low Reynolds numbers. The pressure drop penalty is higher than the heat transfer enhancement obtained by the Onsager–Wien effect in the viscous-force-dominated flows.
4) For the parameters considered in this study, a maximum enhancement of 56 % in the mean Nusselt number is attained with a minimal additional electric power consumption of 8.87 mW.

In this study, a method is proposed to disrupt the laminar viscous and thermal boundary layers in a straight microchannel by using the pseudo-roughness induced by the Onsager–Wien effect. The results indicate that at safe and low applied voltages with minimum power consumption, the Onsager–Wien effect can potentially be used to enhance the heat transfer in a microchannel.

Declaration of Competing Interest

The authors declare that they have no known competing financial interests or personal relationships that could have appeared to influence the work reported in this paper.

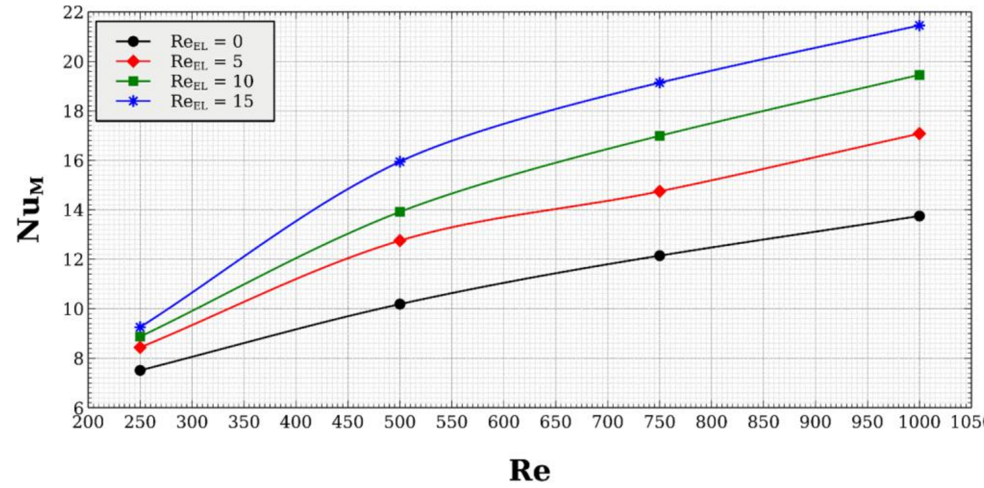

(a)

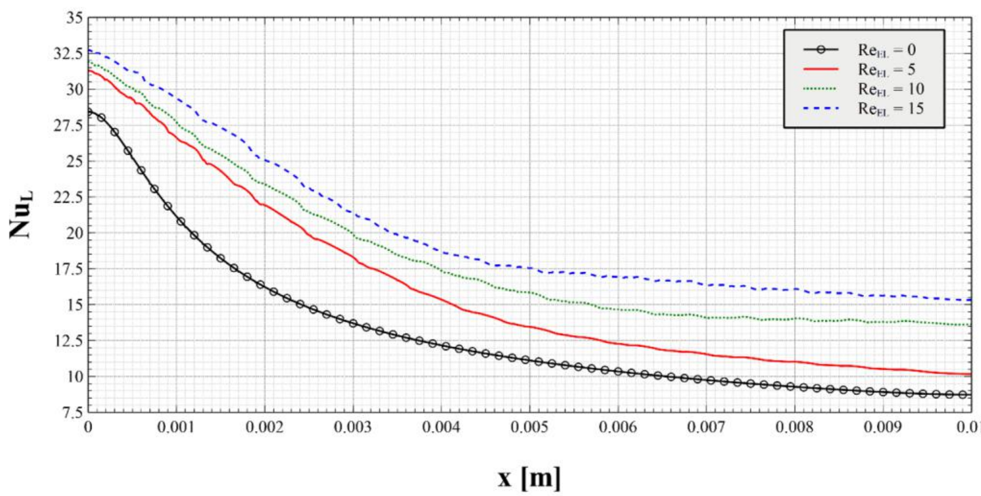

(b)

Fig. 15. (a) Mean Nusselt number variation at $250 \leq Re \leq 1000$ and $0 \leq Re_{EL} \leq 15$, and (b) Local Nusselt number distribution along the bottom wall of the channel at $Re = 1000$ and $0 \leq Re_{EL} \leq 15$.

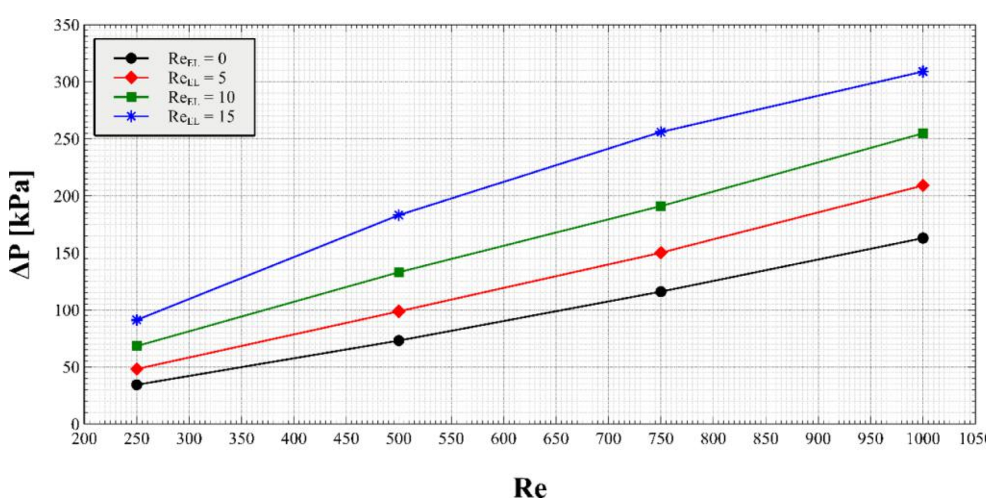

Fig. 16. Pressure drop across the microchannel length at $250 \leq Re \leq 1000$ and $0 \leq Re_{EL} \leq 15$.

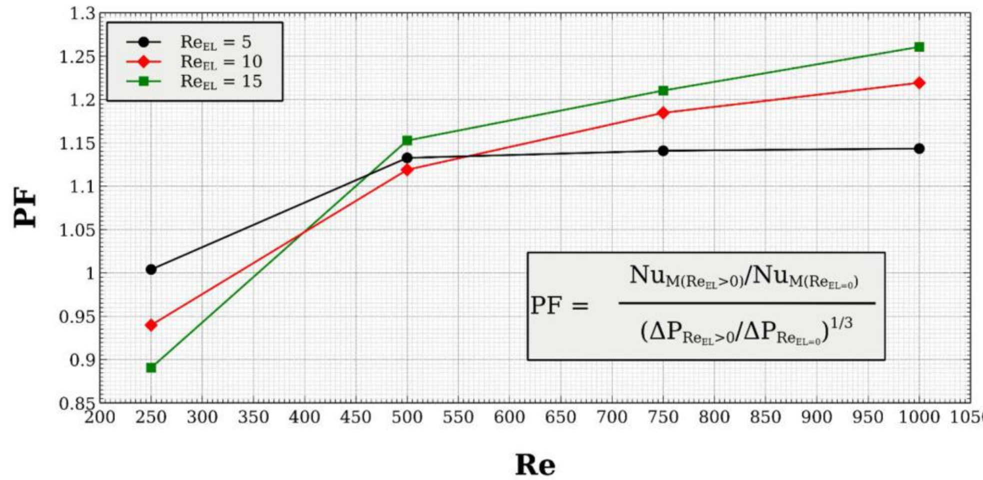

Fig. 17. Performance factor variation at $250 \le Re \le 1000$ and $0 \le Re_{EL} \le 15$.

Table 6
Electric current and power consumption.

	$Re_{EL} = 5$	$Re_{EL} = 10$	$Re_{EL} = 15$
$Re = 250$	$I_{tot} = 2.8899\mu A$	$I_{tot} = 5.8540\mu A$	$I_{tot} = 8.7742\mu A$
	$P_{EL} = 0.9670mW$	$P_{EL} = 3.9173mW$	$P_{EL} = 8.8076mW$
$Re = 500$	$I_{tot} = 2.9132\mu A$	$I_{tot} = 5.8619\mu A$	$I_{tot} = 8.7992\mu A$
	$P_{EL} = 0.9747mW$	$P_{EL} = 3.9228mW$	$P_{EL} = 8.8327mW$
$Re = 750$	$I_{tot} = 2.9301\mu A$	$I_{tot} = 5.8711\mu A$	$I_{tot} = 8.8001\mu A$
	$P_{EL} = 0.9804mW$	$P_{EL} = 3.9290mW$	$P_{EL} = 8.8336mW$
$Re = 1000$	$I_{tot} = 2.9445\mu A$	$I_{tot} = 5.8890\mu A$	$I_{tot} = 8.8335\mu A$
	$P_{EL} = 0.9852mW$	$P_{EL} = 3.9410mW$	$P_{EL} = 8.8671mW$

Data availability

Data will be made available on request.

Acknowledgments

This research was supported by the Chung-Ang University Graduate Research Scholarship in 2022, the National Research Foundation of Korea (NRF) grant funded by the Korea government (MSIT) (No. 2021R1C1C1012119).

References

[1] Z. Zhang, X. Wang, Y. Yan, A review of the state-of-the-art in electronic cooling, E-Prime-Adv. Electrical Eng. Electron. Energy 1 (2021), 100009.
[2] S.G. Kandlikar, History, advances, and challenges in liquid flow and flow boiling heat transfer in microchannels: a critical review, J. Heat Transfer 134 (2012).
[3] N.A.C. Sidik, M.N.A.W. Muhamad, W.M.A.A. Japar, Z.A. Rasid, An overview of passive techniques for heat transfer augmentation in microchannel heat sink, Int. Commun. Heat Mass Transfer 88 (2017) 74–83.
[4] C.-Y. Lee, W.-T. Wang, C.-C. Liu, L.-M. Fu, Passive mixers in microfluidic systems: a review, Chem. Eng. J. 288 (2016) 146–160.
[5] A. Banerjee, A.K. Nayak, B. Weigand, Enhanced mixing and flow reversal in a modulated microchannel, Int. J. Mech. Sci. 155 (2019) 430–439.
[6] M. Gad-el-Hak, The MEMS Handbook, CRC Press, 2001.
[7] J.S. Goodling, Microchannel heat exchangers: a review, in: High Heat Flux Engineering II, 1993, pp. 66–82.
[8] J. Gao, Z. Hu, Q. Yang, X. Liang, H. Wu, Fluid flow and heat transfer in microchannel heat sinks: modelling review and recent progress, Therm. Sci. Eng. Prog. (2022), 101203.
[9] H. Sadique, Q. Murtaza, others, Heat transfer augmentation in microchannel heat sink using secondary flows: a review, Int. J. Heat Mass Transf. 194 (2022), 123063.
[10] E. Mandev, E. Manay, Effects of surface roughness in multiple microchannels on mixed convective heat transfer, Appl. Therm. Eng. 217 (2022), 119102, https://doi.org/10.1016/j.applthermaleng.2022.119102.
[11] Y.-H. Pan, R. Zhao, Y.-L. Nian, W.-L. Cheng, Numerical study on heat transfer characteristics of a pin–fin staggered manifold microchannel heat sink, Appl. Therm. Eng. 219 (2023), 119436, https://doi.org/10.1016/j.applthermaleng.2022.119436.
[12] R. A, S. Chakraborty, Microchannel heat sink with microstructured wall — a critical study on fluid flow and heat transfer characteristics, Therm. Sci. Eng. Prog. 38 (2023), 101613, https://doi.org/10.1016/j.tsep.2022.101613.
[13] M.M. Alqarni, E.E. Mahmoud, E.A. Algehyne, T. Saeed, A.S. Berrouk, M. Ibrahim, Numerical evaluation of the effect of nano-additive type on the second-law performance of γ-AlOOH nano-fluid flow in a wavy microchannel, Chem. Eng. Commun. 210 (2023) 536–548, https://doi.org/10.1080/00986445.2021.1974412.
[14] T. Hou, D. Xu, Pressure drop and heat transfer performance of microchannel heat exchangers with elliptical concave cavities, Appl. Therm. Eng. 218 (2023), 119351, https://doi.org/10.1016/j.applthermaleng.2022.119351.
[15] S. Sabzpoushan, M. Sabouri, Secondary flow through lateral passages to improve hydrothermal performance of liquid-cooled microchannel heat sinks, Appl. Therm. Eng. 227 (2023), 120009, https://doi.org/10.1016/j.applthermaleng.2023.120009.
[16] Y. Wang, Q. Zhong, R. Hua, L. Cheng, C. Wang, H. He, F. Chen, Z. Ma, Ultrasonic vibration-assisted stamping of serpentine micro-channel for titanium bipolar plates used in proton-exchange membrane fuel cell, Materials 16 (2023), 3461, https://doi.org/10.3390/ma16093461.
[17] D. Li, W. Zuo, Q. Li, G. Zhang, K. Zhou, Effects of pulsating flow on the performance of multi-channel cold plate for thermal management of lithium-ion battery pack, Energy 273 (2023), 127250, https://doi.org/10.1016/j.energy.2023.127250.
[18] B. Shankar Goud, P. Pramod Kumar, B.S. Malga, Induced magnetic field effect on MHD free convection flow in nonconducting and conducting vertical microchannel walls, Heat Transfer 51 (2022) 2201–2218, https://doi.org/10.1002/htj.22396.
[19] Y. Wang, G. Xia, R. Li, Q. Li, Z. Yan, Heat transfer enhancement in porous wall mini-channel heat sinks utilizing electric field: an experimental study, Int. J. Heat Mass Transf. 203 (2023), 123803, https://doi.org/10.1016/j.ijheatmasstransfer.2022.123803.
[20] G. Lalagi, P.B. Nagaraj, M. Veerabhadrappa Bidari, R.N. Hegde, Influence of design of microchannel heat exchangers and use of nanofluids to improve the heat transfer and pressure drop characteristics: a review, Int. J. Ambient Energy 43 (2022) 6849–6877, https://doi.org/10.1080/01430750.2022.2056918.
[21] J. Gao, Z. Hu, Q. Yang, X. Liang, H. Wu, Fluid flow and heat transfer in microchannel heat sinks: modelling review and recent progress, Therm. Sci. Eng. Prog. 29 (2022), 101203, https://doi.org/10.1016/j.tsep.2022.101203.
[22] H. Sadique, Q. Murtaza, Samsher, Heat transfer augmentation in microchannel heat sink using secondary flows: a review, Int. J. Heat Mass Transf. 194 (2022), 123063, https://doi.org/10.1016/j.ijheatmasstransfer.2022.123063.
[23] H. Moayedi, N. Amanifard, H.M. Deylami, A simple correlation for predicting the material parameter in micropolar modeling of EHD-enhanced forced convection through a flat channel, J. Electrostat. 103 (2020), 103408.
[24] H.M. Deylami, Effects of EHD on the flow and heat transfer characteristics in a rectangular corrugated channel, Heat Mass Transf. 55 (2019) 3711–3720.
[25] M.C. Ke, J.C. Leong, F.C. Lai, Electrohydrodynamically enhanced forced convection in a horizontal channel by nonsymmetric electric field, J. Thermophys. Heat Trans. 34 (2020) 784–791.
[26] H. Moayedi, Evaluation of the effect of an asymmetric electric field on the electrohydrodynamic enhanced forced convection in a double-wall-heated channel by Q criterion, Eur. Phys. J. Plus 136 (2021) 1–22.
[27] H. Moayedi, N. Amanifard, H.M. Deylami, Evaluation of using micropolar fluid approach for the EHD-enhanced forced convection through a rectangular channel using multiple electrode arrangements, Appl. Therm. Eng. 159 (2019), 113857.
[28] A. Saadatmand, M. Goharkhah, A.M. Nejad, Heat transfer enhancement in mini channel heat sinks utilizing corona wind: a numerical study, Int. J. Heat Mass Transf. 182 (2022), 121970.
[29] J.-S. Leu, J.-Y. Jang, Y.-H. Wu, Three-dimensional electrohydrodynamic enhanced water evaporation using needle-arrayed electrodes, Heat Transfer Eng. 41 (2020) 1921–1937.

[30] C. Qiu, W. Zhou, L. Long, P. Lv, S. Martynenko, L. Yanovskiy, Forced convection heat transfer of aviation kerosene enhanced by electric field in a circular channel, Appl. Therm. Eng. 197 (2021), 117333.
[31] P. Atten, J. Seyed-Yagoobi, Electrohydrodynamically induced dielectric liquid flow through pure conduction in point/plane geometry, IEEE Trans. Dielectr. Electr. Insul. 10 (2003) 27–36.
[32] S.-I. Jeong, J. Seyed-Yagoobi, P. Atten, Theoretical/numerical study of electrohydrodynamic pumping through conduction phenomenon, IEEE Trans. Ind. Appl. 39 (2003) 355–361.
[33] S.I. Jeong, J. Seyed-Yagoobi, Fluid circulation in an enclosure generated by electrohydrodynamic conduction phenomenon, IEEE Trans. Dielectr. Electr. Insul. 11 (2004) 899–910.
[34] Y. Feng, J. Seyed-Yagoobi, Understanding of electrohydrodynamic conduction pumping phenomenon, Phys. Fluids 16 (2004) 2432–2441.
[35] Y. Feng, J. Seyed-Yagoobi, Electrical charge transport and energy conversion with fluid flow during electrohydrodynamic conduction pumping, Phys. Fluids 19 (2007), 57102.
[36] C.-W. Lin, J.-Y. Jang, 3-D numerical analysis for fluid flow and heat transfer in a micro chip by using an electro-hydrodynamic micro-pump, in: International Conference on Nanochannels, Microchannels, and Minichannels, 2005, pp. 215–221.
[37] M.R. Pearson, J. Seyed-Yagoobi, Electrohydrodynamic conduction driven single- and two-phase flow in microchannels with heat transfer, J. Heat Transfer 135 (2013).
[38] M.R. Pearson, J. Seyed-Yagoobi, Single-and two-phase flow in microchannels with heat transfer and driven by an EHD conduction pump, in: ASME International Mechanical Engineering Congress and Exposition, 2011, pp. 937–952.
[39] V.K. Patel, J. Seyed-Yagoobi, Micro-scale two-phase flow heat transport device driven by electrohydrodynamic conduction pumping. Heat Transfer Summer Conference, 2013. V002T04A016.
[40] M. Pearson, Micro-scale EHD Conduction-Driven Pumping and Heat Transfer Enhancement in Single-and Two-phase Systems, Illinois Institute of Technology, 2011.
[41] R.D. Selvakumar, D. Zhonglin, J. Wu, Heat transfer intensification by EHD conduction pumping for electronic cooling applications, Int. J. Heat Fluid Flow 95 (2022), 108972.
[42] N. Nourdanesh, S. Hossainpour, E. Esmaeilzadeh, Experimental investigation of heat transfer enhancement in an open-channel flow with dielectric fluid using electrohydrodynamic conduction pumps concept, Appl. Therm. Eng. 157 (2019), 113711, https://doi.org/10.1016/j.applthermaleng.2019.04.121.
[43] M. Jafari, N. Farrokhi, E. Esmaeilzadeh, Effects of working temperature and fluid physical properties on heat transfer enhancement in conduction pumping: an experimental study, Int. J. Therm. Sci. 156 (2020), 106471, https://doi.org/10.1016/j.ijthermalsci.2020.106471.
[44] N. Nourdanesh, S. Hossainpour, K. Adamiak, Numerical simulation and optimization of natural convection heat transfer enhancement in solar collectors using electrohydrodynamic conduction pump, Appl. Therm. Eng. 180 (2020), 115825, https://doi.org/10.1016/j.applthermaleng.2020.115825.
[45] Z. Du, P.A. Vazquez, J. Wu, Heat transfer enhancement by electrohydrodynamic conduction pumping in a mini-channel, Available at SSRN, 2023 pp. 1–7.
[46] D.V. Fernandes, D.S. Cho, Y.K. Suh, Electrohydrodynamic flow of dielectric liquid around a wire electrode-effect of truncation of Onsager function, IEEE Trans. Dielectr. Electr. Insul. 21 (2014) 194–200.
[47] G. Xia, L. Chai, H. Wang, M. Zhou, Z. Cui, Optimum thermal design of microchannel heat sink with triangular reentrant cavities, Appl. Therm. Eng. 31 (2011) 1208–1219.
[48] M. Mirzaei, M. Saffar-Avval, Enhancement of convection heat transfer using EHD conduction method, Exp. Therm. Fluid Sci. 93 (2018) 108–118.
[49] A. Castellanos, Electrohydrodynamics, Springer Science & Business Media, 1998.
[50] A. Castellanos, Coulomb-driven convection in electrohydrodynamics, IEEE Trans. Electr. Insul. 26 (1991) 1201–1215, https://doi.org/10.1109/14.108160.
[51] 1 Gaz ionises et plasmas, in: Physique Des Plasmas, Vol. I, EDP Sciences, 1994, pp. 1–82, doi: 10.1051/978-2-7598-0287-6.c003.
[52] Y.K. Suh, Modeling and simulation of ion transport in dielectric liquids-Fundamentals and review, IEEE Trans. Dielectr. Electr. Insul. 19 (2012) 831–848.
[53] L. Onsager, Deviations from Ohm's law in weak electrolytes, J. Chem. Phys. 2 (1934) 599–615.
[54] J. Wu, P. Traoré, A finite-volume method for electro-thermoconvective phenomena in a plane layer of dielectric liquid, Numer. Heat Transf. A: Appl. 68 (2015) 471–500.
[55] P.A. Vázquez, M. Talmor, J. Seyed-Yagoobi, P. Traoré, M. Yazdani, In-depth description of electrohydrodynamic conduction pumping of dielectric liquids: physical model and regime analysis, Phys. Fluids 31 (2019), 113601.
[56] C. Chen, J.-T. Teng, C.-H. Cheng, S. Jin, S. Huang, C. Liu, M.-T. Lee, H.-H. Pan, R. Greif, A study on fluid flow and heat transfer in rectangular microchannels with various longitudinal vortex generators, Int. J. Heat Mass Transf. 69 (2014) 203–214, https://doi.org/10.1016/j.ijheatmasstransfer.2013.10.018.
[57] G. Croce, P. D'Agaro, Numerical simulation of roughness effect on microchannel heat transfer and pressure drop in laminar flow, J. Phys. D: Appl. Phys. 38 (2005), 1518.
[58] M. Kadivar, D. Tormey, G. McGranaghan, CFD of roughness effects on laminar heat transfer applied to additive manufactured minichannels, Heat Mass Transf. (2022), https://doi.org/10.1007/s00231-022-03268-1.
[59] H. Lu, M. Xu, L. Gong, X. Duan, J.C. Chai, Effects of surface roughness in microchannel with passive heat transfer enhancement structures, Int. J. Heat Mass Transf. 148 (2020), 119070.
[60] F. Moukalled, L. Mangani, M. Darwish, The finite volume method in computational fluid dynamics, in: An Advanced Introduction with OpenFoam® and Matlab®, Springer, New York, 2016, Recuperado de http://www.didropraktikum.narod.ru/moukalled-et-al-FVM-OpenFOAM-Matlab.Pdf.
[61] B. van Leer, Towards the ultimate conservative difference scheme, J. Comput. Phys. 135 (1997) 229–248.
[62] T. Holzmann, Mathematics, numerics, derivations and OpenFOAM®,, Holzmann CFD, Leoben, Germany, 2016.
[63] R.J. Phillips, Microchannel heat sinks, in: Advances in Thermal Modeling of Electronic Components, 1990.
[64] M.E. Steinke, S.G. Kandlikar, Single-phase liquid friction factors in microchannels, Int. J. Therm. Sci. 45 (2006) 1073–1083.
[65] I. Roghair, M. Musterd, D. van den Ende, C. Kleijn, M. Kreutzer, F. Mugele, A numerical technique to simulate display pixels based on electrowetting, Microfluid Nanofluidics. 19 (2015) 465–482.
[66] U.K. Seth, Message Passing Interface parallelization of a multi-block structured numerical solver, in: Application to the numerical simulation of various typical Electro-Hydro-Dynamic flows, Poitiers, 2019.